Wavelet Analysis and its Application to Modulation Characterization

Craig P. Lusk

Thesis submitted to the Faculty of the

Virginia Polytechnic Institute and State University

in partial fulfillment of the requirements for the degree of

Master of Science

in

Engineering Mechanics

Muhammad R. Hajj, Chair

Scott L. Hendricks

Saad A. Ragab

May 7, 1999

Blacksburg, Virginia

Keywords: Wavelets, Waves, Modulation, Hydrodynamic Stability, Mixing Layers

Wavelet Analysis and its Application to Modulation Characterization

Craig P. Lusk

(ABSTRACT)

Wavelet analysis and its advantages in determining time-varying characteristics are discussed. The Morlet wavelet is defined and procedures for choosing its parameters are described. The recovery of modulation characteristics using the Morlet wavelet is demonstrated. Hydrodynamic linear stability is reviewed and its application to steady and unsteady mixing layers is discussed. Modulation effects are demonstrated by using the magnitude and phase of the wavelet coefficients. The time-varying characteristics of the most unstable modes are determined using the real part of the wavelet coefficients. It is found that mean flow unsteadiness increases the amplitude and phase modulation of the mixing layers. Synchronized variations of the two most unstable modes, the fundamental and the subharmonic, are also observed in the region of subharmonic growth. In a second application of wavelet analysis, the phase lag of the wavelet coefficients is used to determine the phase relation between the fundamental and the subharmonic in acoustically forced mixing layers. The results show that selective forcing affects the time-variations of the phase relation. In a third application, the magnitude and phase of the wavelet coefficients are used to decompose propagating waves measured at a single location.

Dedication

To my wife, Mary

Acknowledgements

I am deeply grateful for the long hours of work of Dr. Muhammad Hajj in advising me in the preparation of this thesis. Without his help, none of this would have been possible. I am also grateful to Don Jordan for his help in getting me started in understanding the wavelet transform and its implementation. I also appreciate the suggestions and help of Dr. Scott Hendricks and Dr. Saad Ragab during the course of my Masters program and the writing of this thesis. In addition, I appreciate the helpful discussions with Demetri Stamos and Dr. Demetri Telionis on the material in Chapter 6. I cannot say enough to express my gratitude to my wife, Mary, for her patience and support while I worked on this thesis. Her professionalism and commitment to excellence are an example to me. Finally, I want to say how much my son Kyle has enriched my life.

Contents

List of Figures

Chapter 1

Introduction

Time-varying systems that have transient, nonstationary or modulation characteristics are present in many phenomena. Examples of such phenomena can be observed in turbulent or transitioning flows, fluid-structure interactions and structural vibrations. The Fourier transform (FT) is not well suited to examine the transient, nonstationary or modulation characteristics of these phenomena. The main reason is the requirement of averaging over the whole length of the record when applying the Fourier Transform. Gabor (1946) defined the Short-Time Fourier Transform (STFT), which overcomes this requirement. The STFT is obtained by applying a single analysis window of limited extent to the signal. Thus, the STFT yields a two-dimensional function in a time-frequency plane. It should be noted that any analysis based on the STFT depends on the window. The Wavelet Transform provides an alternative to the STFT. In contrast to the STFT which uses a single window, the Wavelet Transform uses short windows at high frequencies and long windows at low frequencies.

This analysis is very advantageous in cases where the signal is composed of high-frequency components of short durations and low-frequency components of long durations, which is often the case in many signals related to fluid flows and fluid-structure interactions.

In wavelet analysis, the signal is transformed from the time domain to a time-scale domain. On one hand, a signal in the time domain has information about the magnitude of a signal at a specific instant. On the other hand, a signal in the Fourier domain has information about the magnitude of the signal at a specific frequency. In wavelet analysis, information about the magnitude of a signal is conveyed in a time-scale domain. The magnitude of the wavelet at a specific scale and time is dependent on a specifically weighted range of frequencies and times. Thus, time variations in the frequency and amplitude content of a signal may be captured in a single scale.

In this work, we stress the use of wavelet analysis in recovering the amplitude and phase modulations. These modulations are often found in systems involving nonlinear interactions between different frequency components. They take place in many phenomena, including deep water waves (Yuen & Lake 1975), waves in plasmas (Kim *et. al.* 1980) and transition to turbulence (Miksad *et. al.* 1980). A modulated wave is characterized by its carrier frequency, amplitude and phase modulation. The relative phase between amplitude and phase modulations and the modulation levels play an important role in energy redistribution to the sidebands and their structures. A measure of the modulation characteristics is important to establish physical interpretation of many phenomena. In chapter 2, wavelet analysis is presented, the Morlet wavelet is defined and procedures are outlined for appropriate choice of its

parameters. The implementation process is described and the wavelet transform is illustrated with a variety of amplitude and frequency modulated signals. In chapter 3, hydrodynamic linear stability is reviewed. It is shown that the mean flow unsteadiness produces amplitude and phase modulations in shear flows. The experimental setup for the steady and unsteady mixing layers is briefly described. In chapter 4, wavelet analysis is performed on steady and unsteady mixing layers to help validate the conclusions of chapter 3. In chapter 5, the phase of the wavelet is used to determine the phase relation between the fundamental and subharmonic components and to qualify the effects of this relation on the subharmonic growth. In chapter 6, the magnitude and phase of the wavelet coefficients are used to decompose propagating waves. In chapter 7, conclusions resulting from this work are presented.

Chapter 2

Signal Modulation with Wavelet Analysis

In this chapter, the wavelet transform is defined. Specific issues related to the computational procedure for its implementation are discussed. Analytic forms of signals are used to validate the computational procedure. These signals are also used to show the usefulness of the wavelet transform in characterizing amplitude and phase modulations.

2.1 Wavelet Analysis

2.1.1 Definitions

The continuous wavelet transform, $W(a,\tau)$, of a function, $g(t)$, is defined as the convolution of $g(t)$ and the complex conjugate of a wavelet family, $\Psi(a,t)$:

$$W(a,\tau) = \int_{-\infty}^{\infty} g(t)\Psi^*(a,t-\tau)dt \tag{2.1}$$

where t is the integration variable and the superscript $*$ denotes the complex conjugate. The wavelet family, $\Psi(a,t)$, is obtained by shifting and scaling a mother wavelet, $\Psi(a=1,t)$ in accordance with

$$\Psi(a,t-\tau) = p(a)\Psi(\frac{t-\tau}{a}) \tag{2.2}$$

In this equation, a is a scale dilation parameter that corresponds to the size of the wavelet and would thus be related to a frequency range and τ is a translation parameter. The function $p(a)$ is a scale weighting function that can be chosen differently for different purposes. Usually, $p(a)$ is chosen to be proportional to $a^{-\frac{1}{2}}$, so that all wavelets have the same energy at each scale. Other choices for $p(a)$ include a^{-1} and $a^0 = 1$. In this work, the weighting function $p(a)$ is chosen as

$$p(a) = 2(\frac{\sqrt{2\pi}}{a}) \tag{2.3}$$

This choice produces wavelets with scales having equal magnitudes at the peak frequency.

The relation between scale and peak frequency will be discussed later. The reason for this choice is to allow for convenient normalization of the carrier frequency and modulating components. Transforming the convolution in equation 2.1 to frequency domain and applying the Inverse Fourier Transform (IFT), the wavelet coefficients for this choice of $p(a)$ can be calculated as

$$W(a,\tau) = 2\sqrt{2\pi}\int_{-\infty}^{\infty} \hat{g}(f)(\hat{\Psi}^*(a,f))e^{i2\pi f\tau}df \tag{2.4}$$

where $\hat{\Psi}(a,f) = \hat{\Psi}(af)$ is the Fourier transform of $\Psi(\frac{t}{a})$ and $\hat{g}(f)$ is the Fourier transform of $g(t)$. Performing the Wavelet Transform in the Fourier domain and using equation 2.4 is very useful for efficient numerical computation of the wavelet coefficients which can be real or complex.

To perform the Inverse Fourier Transform, the wavelet must be admissible, i.e. it must satisfy finite energy criteria, namely it must have a zero DC offset and finite bandwidth and gain. This condition insures that the integral in equation 2.4 is finite. Equivalently, the admissibility condition can be expressed in the time domain as the requirement that the wavelet must have zero mean and finite temporal support, i.e. its magnitude must go to zero as time becomes large.

One common complex wavelet is the Morlet wavelet, where the mother wavelet is given by the product of a complex sinusoid and a Gaussian function

$$\Psi(t) = e^{i2\pi f_0 t}e^{\frac{-(2\pi f_\psi t)^2}{2}} \tag{2.5}$$

where f_0 is the peak frequency of the wavelet and f_ψ is an attenuation parameter that

determines the temporal support of the mother wavelet.

The Fourier Transform (FT) of the mother Morlet wavelet in equation 2.5 is given by

$$\hat{\Psi}(f) = (2\pi)^{\frac{-1}{2}} e^{\frac{-(f-f_0)^2}{2f_\psi^2}} \tag{2.6}$$

Thus, the FT of the mother Morlet wavelet is a Gaussian curve, which is characterized by a peak frequency f_0 and a standard deviation, f_ψ. Based on equations 2.2 and 2.5, the family of Morlet wavelets in the time domain is given by

$$\Psi(a,t) = 2(\frac{\sqrt{2\pi}}{a}) e^{\frac{i2\pi f_0 t}{a}} e^{-(\frac{2\pi f_\psi t}{a})^2/2} \tag{2.7}$$

The FT of the complex conjugate of the wavelet family is then given by

$$\hat{\Psi}^*(a,f) = 2e^{\frac{-(af-f_0)^2}{2f_\psi^2}} \qquad f \geq 0 \tag{2.8}$$

$$\hat{\Psi}^*(a,f) = 0 \qquad f < 0 \tag{2.9}$$

The factor of 2 in equation 2.9 results from considering the positive frequency components only. Based on equation 2.9, the peak frequency, f_p, and the standard deviation of the frequency domain wavelets are given by $\frac{f_0}{a}$ and $\frac{f_\psi}{a}$. Thus, the ratio of peak frequency to standard deviation is invariant with scale. This ratio defined as,

$$\gamma = f_0/f_\psi, \tag{2.10}$$

also determines the number of cycles that occur in one standard deviation of the Gaussian curve in its time domain representation.

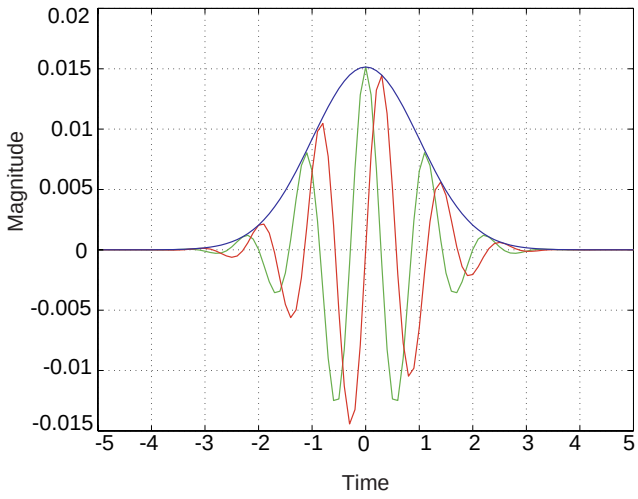

Figure 2.1: The Morlet wavelet, $\Psi(a,t)$, the magnitude (blue) and the real (green) and imaginary (red) parts

Generic shapes of the Morlet wavelet in the time and frequency domains are plotted in figure 2.1 and 2.2, respectively. Simply for illustrative reasons, the generic plots shown in figures 2.1 and 2.2 correspond to different scales. The time domain plot (figure 2.1) shows the magnitude and the real and imaginary parts of the wavelet. Note that the real part is an even function and the imaginary part is odd. This means that the Fourier Transform of the complex conjugate of the wavelet, shown in figure 2.2, is real. As the scale, a, increases, the width of the Gaussian envelope in the time domain increases and its magnitude decreases. In the Fourier domain, an increase in scale corresponds to a decrease in the peak frequency and a decrease in the bandwidth of the wavelet. In the plots shown, the cycle parameter, γ, is 5.5. However, depending on the nature of the data to be analyzed, a different value of γ may be chosen.

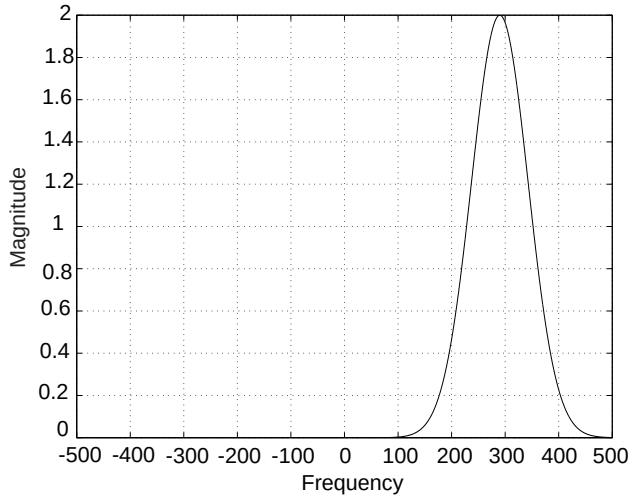

Figure 2.2: Morlet Wavelet in Fourier domain

2.1.2 Choice of Wavelet Parameters

Optimal choices of wavelet parameters should be derived from the nature of the data to be studied. Three quantities must be chosen. The first is the cycle parameter, γ, which determines the frequency bandwidth and temporal support of the wavelet. The second is the peak frequency, f_0, of the mother wavelet, which has the smallest temporal support, the highest peak frequency and the largest frequency bandwidth. This choice also determines the value of the scale index, a, that will correspond to a particular peak frequency. The third quantity is the peak frequency, f_l, of the scale which has the largest temporal support, lowest peak frequency and smallest frequency bandwidth. Essentially, γ is chosen to give the desired resolution of the wavelet family with respect to time and frequency. The peak frequency parameters, f_0 and f_l, are chosen based on the frequency range that is of interest in the signal.

The range of values of f_0, f_l and γ that would satisfy the admissibility condition must be determined.

To do this, we first consider the requirement that the wavelets have a zero DC value. In equation 2.9, we let the magnitude of the DC component of the wavelet be equal to some small value, $\epsilon_{DC} \ll 1$, and we solve for the largest admissible standard deviation, f_ψ.

$$f_\psi \leq \frac{af - f_0}{\pm\sqrt{-2ln[\epsilon_{DC}]}} \tag{2.11}$$

Using equations 2.6 and equation 2.11, we find an equation for the smallest admissible value for γ.

$$\gamma \geq \frac{\pm f_0\sqrt{-2ln[\epsilon_{DC}]}}{af - f_0} \tag{2.12}$$

At the DC value, $f = 0$, the values of γ that will yield a DC value of at most ϵ_{DC} are given by

$$\gamma \geq |\sqrt{-2ln[\epsilon_{DC}]}| \tag{2.13}$$

Thus, in order for the DC value to go to zero, γ must go to infinity, an obviously unfeasible requirement. In practical terms, it is sufficient that ϵ_{DC} be negligibly small. Alternatively, if the signal $g(t)$ has a zero mean, then the product of $\hat{g}(f)$ and $\hat{\Psi}(a, f)$ will have a zero mean and will thus be admissible (Teolis 1997).

Next, we analyze the requirement that the wavelets have finite temporal support. This means that each wavelet should have a negligible magnitude at a time larger than some specified time, t_s. The attenuation of the wavelet with time is determined by the Gaussian portion of

equation 2.8. Thus, that part of the equation is set equal to a small magnitude, $\epsilon_t \ll 1$. We then solve for f_ψ to find its smallest permissible value, which is given by

$$f_\psi \geq \frac{a}{2\pi t_s}\sqrt{-2ln[\epsilon_t]} \tag{2.14}$$

Using equations 2.10 and 2.14 and the relation between scale and peak frequency in other terms, we find the peak frequency, f_p, that will have a magnitude, ϵ_t, at a time, t_s, for a cycle parameter of γ. This relation is given by

$$f_p = \frac{\gamma\sqrt{-2ln[\epsilon_t]}}{2\pi t_s} \tag{2.15}$$

Requiring that the largest scale, $f_p = f_l$, has a magnitude no greater than ϵ_t at a time, t_s, will satisfy this requirement for all scales i.e.

$$f_l \geq \frac{\gamma\sqrt{-2ln[\epsilon_t]}}{2\pi t_s} \tag{2.16}$$

Note that no scale can have a magnitude, $\epsilon_t = 0$, in finite time. However, we also observe that ϵ_t may become very small in a short time.

Finally, we consider the requirement that the wavelets should not be aliased. We solve equation 2.8 for the peak frequency of the mother wavelet, f_0,

$$f_0 = af - f_\psi\sqrt{-2ln[\hat{\Psi}^*(a,f)]}. \tag{2.17}$$

Equation 2.17 can be expressed in terms of γ instead of f_ψ using equation 2.6

$$f_0 \leq \frac{af\gamma}{\gamma + \sqrt{-2ln[\epsilon_N]}} \tag{2.18}$$

The mother wavelet is the scale that will have the largest magnitude at the Nyquist frequency. Thus, it is sufficient to require that the magnitude of the mother wavelet at the Nyquist frequency, $\Psi(a = 1, f = f_N)$, be very small. If we define ϵ_N as the maximum allowable magnitude at the Nyquist frequency, we determine the largest allowable peak frequency, $f_p = f_0$, for the mother wavelet, $a = 1$

$$f_0 \leq \frac{f_N\gamma}{\gamma + \sqrt{-2ln[\epsilon_N]}} \tag{2.19}$$

It is obvious that every scale will be aliased by some small amount. Likewise, it has been shown that no Morlet wavelet will go to zero in finite time or have zero mean. On the other hand, for most practical purposes, it is not hard to determine parameters that give adequate results.

A practical approach for determining the wavelet parameters depends on the frequency range of interest and the need to balance the temporal support of the wavelet and its bandwidth. An important phenomenon that occurs due to the temporal support of the wavelets is a wraparound effect. This affects wavelet coefficients calculated at times less than the temporal support, t_s, from the first and last data points. The effect is caused by performing the circular convolution using the FFT. This means that the input signal, $g(t)$ is considered to be periodic. Since this is not generally the case, there is an apparent discontinuity in the signal at the first and last data points. It also means that data from the end of the

signal is used to compute the coefficients in the beginning of the signal and vice-versa. This effect is significantly reduced by the time that $\epsilon_t = .01$. This effect is described in Jordan *et. al.* (1997) and is easily compensated for by simply discarding the affected coefficients. A related phenomenon occurs at any discontinuity in the signal. The discontinuity will be smoothed over the temporal support of the wavelet. In order to appropriately locate the time that such discontinuities occur, it is desirable that the temporal support, t_s be small. From equation 2.16, we can conclude that at a given peak frequency the temporal support is directly proportional to γ. Thus, for a high level of temporal resolution, γ, should be small.

Important considerations derive from the bandwidth of the wavelet. At a particular frequency, it may be desirable to either include, or exclude the effects of other frequency components. In order to study modulation effects, the bandwidth must be adequate to include significant modulating components. On the other hand, in order to isolate physically independent phenomena, it may be desirable to have very narrow wavelet bandwidths. It can be shown by writing equation 2.9 in terms of peak frequency, f_p and the cycle parameter, γ, that the bandwidth of a scale is inversely proportional to γ

$$\hat{\Psi}(\frac{f_0}{f_p}, f) = 2e^{\frac{-(f-f_p)^2}{2(\frac{f_p}{\gamma})^2}} \tag{2.20}$$

Thus, in order to have wavelets with narrow bandwidths, the cycle parameter, γ, must be large.

2.1.3 Implementation

Implementation of the wavelet transform consists of three basic processes, input, computation and output. The input required for the wavelet transform consists of the wavelet design parameters and the digital signal, $f[n\Delta t]$, where Δt is the sampling time. In this work, the data to be analyzed in this work was sampled at 1000 Hz and the total length of each record is 4096 data points. The mean has been removed from the data records, thus, the size of ϵ_{DC} is not an important consideration. Also, since we consider the modulation of a fundamental frequency of 215 Hz by a low frequency component of 35 Hz, our scales should at least cover the range of peak frequencies from 35 to 250 Hz.

Since the bandwidth and the temporal support of the wavelet are inversely related, optimal wavelet design requires that the need for temporal resolution be balanced against the need for resolution in the Fourier domain. The three most significant frequency components in the signals analyzed in this work are the fundamental mode at 215 Hz, its subharmonic at 107.5 Hz and the low-frequency modulating component at 35 Hz. We would like to insure in the wavelet we use to investigate the fundamental frequency, 215 Hz, is sufficiently bandlimited to exclude the subharmonic frequency, 107.5 Hz. We would also like to have a temporal resolution such that the time, t_s, of the scale with peak frequency of 35 Hz takes to become very small is on the order of .1 s.

We would like to determine if these two requirements produce compatible restrictions on the cycle parameter γ. Solving equation 2.20 for the cycle parameter, γ, we find that the value

of γ can be specified by requiring that the magnitude of the scale with peak frequency, f_p, to be small at a certain frequency, i.e. $\hat{\Psi}(\frac{f_0}{f_p}, f) = \epsilon$.

$$\gamma \geq \pm \frac{f_p \sqrt{-2ln[\epsilon]}}{f - f_p} \tag{2.21}$$

Thus in equation 2.21, we let $f_p = 215$ and take $\epsilon = .01$ at f = 107.5. This yields a γ value of at least 6.07. Next, we solve equation 2.16 for γ, to determine what the maximum cycle parameter is that will give the specified temporal support at the scale with peak frequency, f_p, of 35 Hz.

$$\gamma \leq \frac{2\pi f_p t_s}{\sqrt{-2ln[\epsilon_t]}} \tag{2.22}$$

In equation 2.22, $f_p = 35$ Hz, the temporal support, $t_s = .1$ s, and we take $\epsilon_t = .0001$. This yields a maximum cycle parameter, γ, of 5.1. Since, we cannot satisfy both criteria specified above, we relax both of them slightly and choose a cycle parameter of $\gamma = 5.5$. This yields an ϵ value of .023 and an ϵ_t value of .0003, which are acceptable.

Now having determined γ, we find using equation 2.20 that the upper bound for the peak frequency of the mother wavelet, $f_0 = 298$ for an ϵ_N value of .001. We take $f_0 = 290$ in our analyses.

The computation consists of generating the family of wavelets consisting of several scales and convolving the signal with each scale. Because convolution in the time domain is the same as multiplication in the Fourier domain, it is computationally more efficient to perform the calculations in the Fourier domain. Thus, the FFT of the digital time series is a first step.

Since analytical expressions are given for the wavelet in both the time domain and the frequency domain, the wavelet Kernel for each scale can be generated in either the time domain or the Fourier domain. Generating the wavelet in the Fourier domain reduces the number of computational operations and is thus more efficient. There are significant reductions in the error associated with computing the transform when the wavelet is generated in the Fourier domain as opposed to the time domain. For instance, in the analysis of a sine wave, the error level in the recovered magnitude when using wavelets sampled in the time domain is of the order of 10^{-3}. This error is reduced to 10^{-9} when the wavelets are sampled in the Fourier domain. This reduction in error can be particularly significant in calculating the phase, especially when the real part of the wavelet coefficients are small. After each wavelet is generated it is multiplied by the Fourier transform of the input signal. Finally, the Inverse Fourier Transform is taken of the product of the wavelet and the Fourier transformed signal to yield the complex wavelet coefficients.

When applied to determine time-variations in a signal, the magnitude, phase and real part of the wavelet coefficients each convey specific information. The amplitude modulation of a signal can be determined from the magnitude of the wavelet coefficients. The phase and frequency modulation can both be determined from the phase of the wavelet coefficients. The real part of the wavelet coefficients represents a filtered version of the signal and conveys information about the time variations of specific components of the signal.

2.2 Examples

In order to validate the computational procedure, analytic signals are used. Because it is the objective of this work, the recovery of modulation parameters is stressed.

2.2.1 Sinusoids

The first analytic signals to be tested are a cosine wave with amplitude A, and a sine wave with amplitude B. The benefits of using both sine and cosine waves will be shown later. They are given by

$$g_c(t) = Acos(2\pi f_g t) \tag{2.23}$$

$$g_s(t) = Bsin(2\pi f_g t) \tag{2.24}$$

In the Fourier domain, $g_c(t)$ is given by $\frac{A}{2}[\delta(2\pi f_g)+\delta(-2\pi f_g)]$ and $g_s(t)$ is given by $\frac{-iB}{2}[\delta(2\pi f_g)-\delta(-2\pi f_g)]$. For these functions, the integrand of equation 2.4 is a linear combination of delta functions. Thus, it only needs to be evaluated at $f = \pm 2\pi f_g$. If a scale, a_0, is chosen so that the peak frequency, f_p of that scale is equal to f_g, $\hat{\Psi}(a_0, f = f_g) = 2$ from equation 2.9 and $\hat{\Psi}(a_0, f = -f_g) = 0$ from equation 2.10. Thus, applying equation 2.4, the wavelet transform of the cosine function at the scale a_0 is

$$W[g_c(t)](a_0, \tau) = Ae^{i2\pi f_g \tau} \tag{2.25}$$

and the wavelet transform of the sine function at the scale a_0 is,

$$W[g_s(t)](a_0, \tau) = -iBe^{i2\pi f_g \tau} \tag{2.26}$$

Thus, for the more general case of $g_m(t) = Ccos(2\pi f_g t + \theta)$ can be written as $Acos(2\pi f_g t) - Bsin(2\pi f_g t)$ i.e. $g_c(t) - g_s(t)$, where $A = Ccos(\theta)$ and $B = Csin(\theta)$. The wavelet transform of $g_m(t)$ is:

$$W[g_m](a_0, \tau) = W[g_c(t)](a_0, \tau) - W[g_s(t)](a_0, \tau) = (A + iB)e^{i2\pi f_g \tau} \tag{2.27}$$

The amplitude and phase of $g_m(t)$ can be recovered from the magnitude and phase of the complex wavelet coefficients. The magnitude of $W[g_m](a_0, \tau)$ is given by

$$|W[g_m](a_0, \tau)| = \sqrt{A^2 + B^2} \tag{2.28}$$

which equals C for all times, τ. The phase of the wavelet coefficients will be time-varying, and is given by

$$\angle W[g_m](a_0, \tau) = atan(B/A) + 2\pi f_g \tau \tag{2.29}$$

The instantaneous frequency, or frequency variation can be obtained from the time derivative of the argument of the wavelet coefficients.

$$FM(\tau) = \frac{d}{d\tau}(\angle W(a_0, \tau))/2\pi \tag{2.30}$$

From the instantaneous frequency, one can define a nominal carrier as

$$\bar{FM} = E[FM(\tau)] \tag{2.31}$$

In the example given above, $FM(\tau)$ is constant, and the phase angle, θ can be recovered by subtracting the carrier, $2\pi \bar{FM}\tau$ from the argument of the wavelet coefficients.

$$\theta = (\angle W[f_m(t)](a_0, \tau) - 2\pi \bar{FM}\tau) \tag{2.32}$$

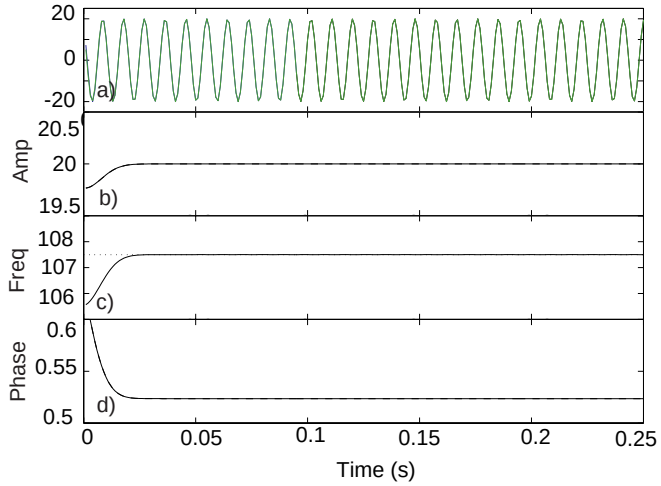

Figure 2.3: Example of signal recovery for $g_m(t) = 20cos(2\pi 107.5t + \frac{\pi}{6})$, using a scale with peak frequency, $f_p = 107.5$. Part a) the original signal (blue) and the recovered signal (green). Part b) the recovered instantaneous magnitude. Part c) the recovered instantaneous frequency. Part d) the recovered phase lag

Figure 2.3 shows a nondimensional numerical example obtained by setting $f_g = 107.5, \theta = \pi/6$ and $C = 20$. Part a shows $g_m(t)$ and the real part of the wavelet coefficients from a scale that has a peak frequency, f_p equal to the carrier frequency, f_g. The results show that the signal (blue) can be recovered from the real part of the wavelet coefficients (green). Part b shows the recovered magnitude, C_r, which is shown to equal to C for all but the initial part of the record. Part c shows the instantaneous frequency, f_r and part d shows the phase lag, $\phi(\tau)$, which likewise show that the signal properties have been recovered. Note that in the first .01 seconds of the record, the recovered values are not equal to the nominal values. This is due to the wraparound effects discussed in section 2.1.2. The results presented here show how the wavelet transform can be used to accurately recover the instantaneous magnitude and phase of a monochromatic wave.

The example given above is now re-examined to illustrate what happens when the peak frequency of the scale is not equal to the frequency of the sinusoid. If the difference between the carrier frequency, f_g and the peak frequency of the wavelet, f_p is ν Hz then the magnitude of the recovered signal is attenuated by $\xi(\nu, f_p)$.

$$\xi(\nu, f_p) = e^{-(\frac{\omega_\psi \nu}{f_p})^2/2} \tag{2.33}$$

Figure 2.4 shows the same signal as in Figure 2.3, but this time the wavelet transform is performed at a scale with peak frequency equal to 100 Hz. This yields $\xi(7.5, 100) = .9184$. Part b shows that the recovered magnitude is in fact equal to $.9184C(= \xi(7.5, 100))C$. Parts c and d show that the calculation of the phase and frequency of the sinusoid were not affected by the change in scale. The fact that the actual frequency of the sinusoid can be found over a range of scales is very powerful, because it implies that the carrier frequency need not be precisely known in order to recover modulation characteristics. Figure 2.5 shows the wavelet coefficients for the signal g_m over a range of scales. Part a of the plot shows the signal, part b shows the magnitude of the wavelet coefficients, part c shows the real part and part d shows the phase of the wavelet coefficients. The plots in figures 2.3b and 2.4b constitute horizontal cross sections of figure 2.5b at ln(a) = 1 and ln(a) = 1.06 respectively. In accordance with equation 2.34, the magnitude of the wavelet coefficients is a maximum at the scale that corresponds to the carrier frequency, f_g, and decreases for all other scales. The time variations observed in parts c and d occur on the time scale of the carrier. The lines of constant phase are vertical, meaning that the same instantaneous phase could be found at all of the scales from ln(a) = 0 to ln(a) = 1.7. This means the carrier frequency of

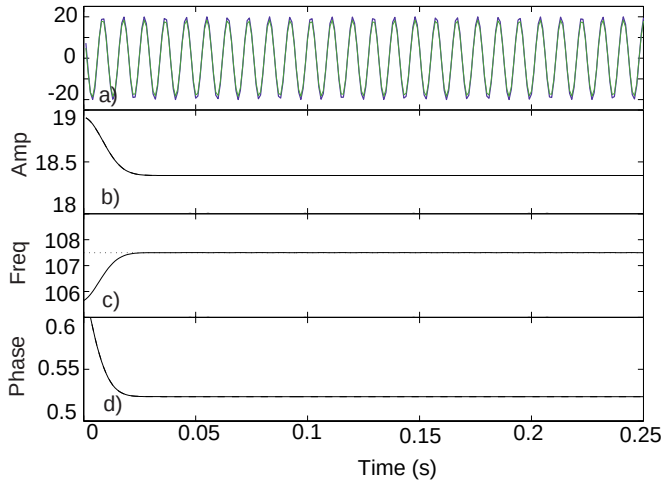

Figure 2.4: Example of signal recovery for $g_m(t) = 20cos(2\pi 107.5t + \frac{\pi}{6})$, at a scale with peak frequency, $f_p = 100$. Part a) the original signal (blue) and the recovered signal (green). Part b) the recovered instantaneous magnitude. Part c) the recovered instantaneous frequency. Part d) the recovered phase lag

this signal could be recovered from any of these scales. The phases at the scales larger than ln(a) equal to 1.7, are determined by wrap around effects, and are not significant. Having demonstrated that the magnitude, phase and frequency of a signal can be recovered even at scales that are not equal to the peak frequency, we proceed to examine polychromatic signals, i.e. signals with many components.

2.2.2 Amplitude Modulation

An amplitude-modulated signal is written as

$$g_a(t) = (A + Bcos[2\pi(\nu t)])cos(2\pi f_g t) \tag{2.34}$$

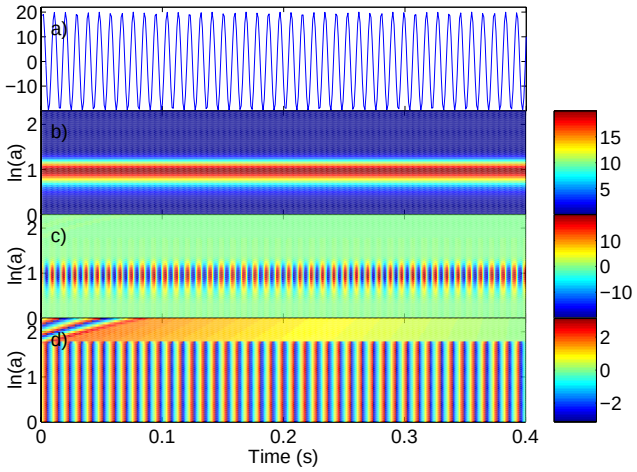

Figure 2.5: Wavelet coefficients for the signal given by $g_m(t) = 20cos(2\pi 107.5t + \frac{\pi}{6})$, part a) the original signal, $g_m(t)$, part b) the magnitude of the wavelet coefficients, part c) the real part of the wavelet coefficients and part d) the phase of the wavelet coefficients

or equivalently,

$$g_a(t) = Acos(2\pi f_g t) + \frac{B}{2}cos[2\pi(f_g + \nu)t] + \frac{B}{2}cos[2\pi(f_g - \nu)t] \tag{2.35}$$

Based on equation 2.27, the wavelet transform is given by

$$W[g_a(t)](a_0, \tau) = Ae^{i2\pi f_g t} + B_W e^{2\pi(f_g+\nu)t} + B_W e^{2\pi(f_g-\nu)t} \tag{2.36}$$

where B_W, based on the arguments presented above, is given by

$$B_W(\tau) = \xi(\nu, f_p)B. \tag{2.37}$$

Figure 2.6 shows the recovery of an amplitude modulated signal with $A = 20$, $B = 5$, $f_g = 215$ and $\nu = 15$. Part a shows the original signal. Part b shows the magnitude of the wavelet coefficients. Parts c and d show the instantaneous frequency and phase lag

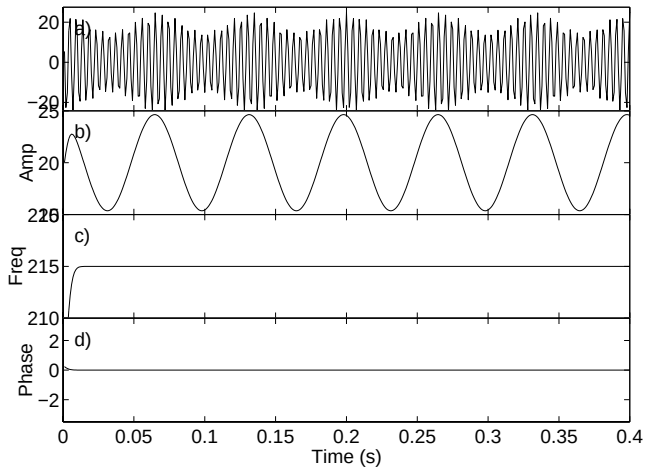

Figure 2.6: Example of signal recovery for $g_a(t) = [20 + 5cos(2\pi 15t)]cos(2\pi 215t)$, at the scale with peak frequency, $f_p = 215$. Part a) the original signal, $g_a(t)$. Part b) the recovered instantaneous magnitude. Part c) the recovered instantaneous frequency. Part d) the recovered phase lag

respectively. Notice that the amplitude modulation does not produce variations in phase or frequency. Also notice that the magnitude of the wavelet coefficients oscillates about a mean value of A = 20 and the amplitude is B_W.

Figure 2.7 shows the power spectrum of the signal shown in figure 2.5 and the power spectra of its modulation. Part a shows the power spectrum of the signal, parts b, c, and d show the spectra of the amplitude, frequency and phase modulations respectively, each normalized by $\xi(\nu, 215)$. Since the power spectra of $g_a(t)$ yields the attenuated rms, normalizing by the attenuation coefficient and $\sqrt{2}$ should return the amplitude modulation exactly. Note that the normalized spectra of the phase and frequency are less than 10^{-7}.

Figure 2.8 shows the wavelet coefficients for a range of scales from ln(a) = 0 to ln(a) =

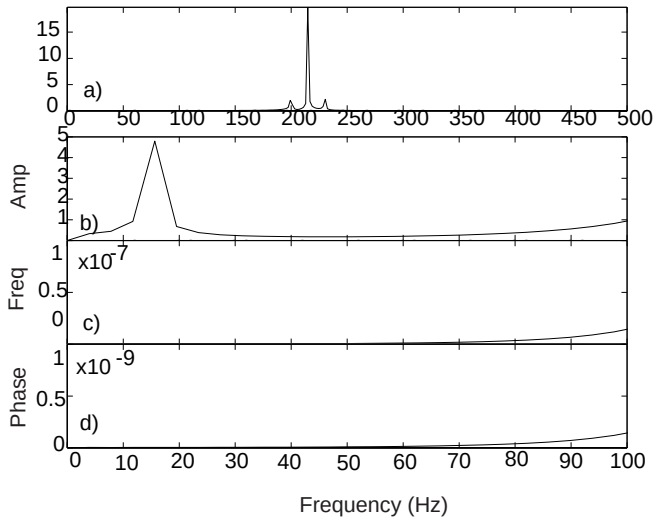

Figure 2.7: Spectra of the modulation of $g_a(t) = [20 + 5cos(2\pi 15t)]cos(2\pi 215t)$, at the scale with peak frequency, $f_p = 215$. Part a) Normalized spectrum of the original signal $g_a(t)$ Part b) Normalized spectrum of amplitude modulation. Part c) Normalized spectrum of frequency modulation. Part d) Normalized spectrum of phase modulation

2. The amplitude modulation causes the variations that appear as the four red ovals in the horizontal band at ln(a) = 0.3 in part b. The range of scales with a carrier frequency of 215 Hz is reduced from the sinusoidal case by the introduction of additional frequency components. Note that by the scale given by ln(a) = 0.6, the component that determines the phase of the scale is not the 215 Hz component but the 200 Hz component.

Unexpected results may occur when the attenuated modulation amplitude, B_W, is greater than the carrier amplitude, A, due to the overmodulation. This occurs any time that the sum of the carrier amplitude and its modulating components go to zero. The magnitude of the wavelet coefficients approaches zero, and hence the phase becomes undefined. This means that the phase may be quite different from nearby values, and a spike may occur in the instantaneous frequency. This phenomenon is illustrated with a signal that has a carrier

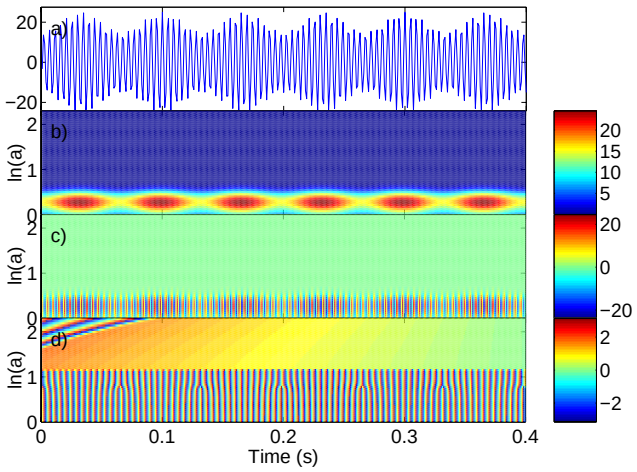

Figure 2.8: Wavelet coefficients for the signal given by $g_a(t) = [20+5cos(2\pi 15t)]cos(2\pi 215t)$, Part a) the signal, $g_a(t)$ Part b) the magnitude of the wavelet coefficients. Part c) the real part of the wavelet coefficients Part d) the phase of the wavelet coefficients.

frequency, $f_0 = 215$ Hz, a carrier amplitude, $A = 20$, a modulation frequency, $\nu = 15$ Hz, and a modulation amplitude, $B = 30$. In Figure 2.9, the signal is plotted in part a and the amplitude, frequency and phase modulations are shown in parts b, c and d, respectively. In figure 2.9.b, we see that the magnitude of the wavelet coefficients produces an alternating sequence of large and small amplitude curves. The large amplitude curves correspond to the times when the carrier amplitude, A, is greater than the attenuated modulating components, $B_W/2[cos(2\pi 200t) + cos(2\pi 230t)]$, and the small amplitude curves correspond to times when the carrier amplitude is less than the attenuated modulating components. There are π jumps in phase when the modulating components become larger than the carrier amplitude and vice versa. The instantaneous frequency at these jumps becomes singular. These singularities introduce errors when the spectra is calculated.

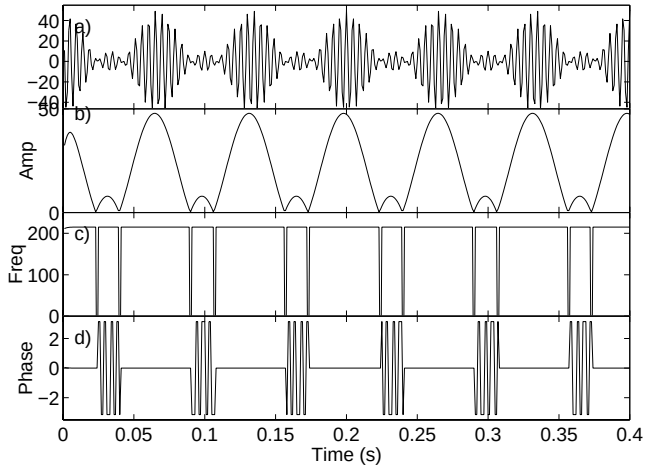

Figure 2.9: Example of signal recovery for $g_a(t) = [20 + 30cos(2\pi 15t)]cos(2\pi 215t)$, Part a) The original signal, $g_a(t)$. Part b) the amplitude modulation. Part c) the frequency modulation. Part d) the phase modulation

The spectra of the overmodulated signal are shown in Figure 2.10. The spectrum of the original signal is shown in part a, the spectra of the amplitude, frequency and phase are shown in parts b, c and d. The spectrum of the signal, figure 2.10.a is not remarkably different than the ordinary amplitude modulated signal shown in figure 2.7.a. The amplitude modulation spectrum, shown in figure 2.10.b, has additional peaks at the harmonics of the modulation frequency. Peaks occur at the harmonics of the modulating frequency in the frequency modulation, shown in figure 2.10.c. The discontinuities in phase make it almost impossible to detect the peaks that occur at harmonics of the modulation frequency in figure 2.10.d.

The wavelet coefficients for the overmodulated signal are plotted over a range of scales in figure 2.11. The original signal is plotted in part a, and the magnitude, real part and phase

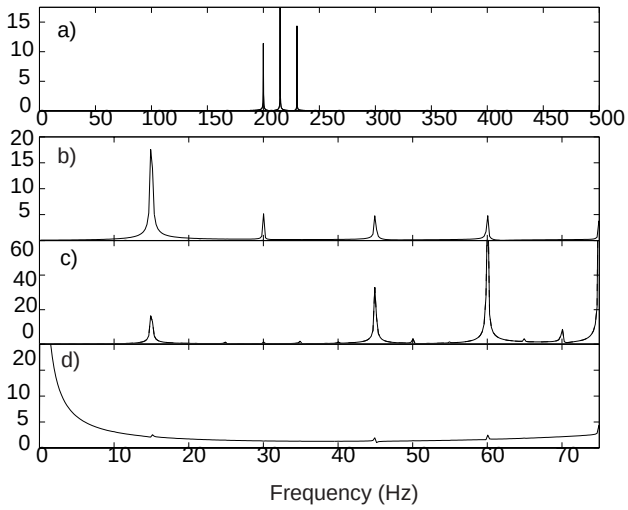

Figure 2.10: Spectra of the modulation of $g_a(t) = [20 + 30cos(2\pi 15t)]cos(2\pi 215t)$, Part a) Normalized spectrum of $g_a(t)$. Part b) Normalized spectrum of amplitude modulation. Part c) Normalized spectrum of the frequency modulation. Part d) Normalized spectrum of the phase modulation

of the wavelet coefficients are shown in parts b, c and d, respectively. In the magnitude of the wavelet coefficients, shown in part b, the colored concentric circles correspond to the large amplitude portions of the signal. There are smaller dark blue circles that correspond to the magnitude of the of the small amplitude portions of the signal. There is a subtle difference between the phase of the overmodulated case, in figure 2.11.d and the phase of the amplitude modulated signal shown in figure 2.8.d. The carrier frequency of the scales changes from 215 Hz to 200 Hz occurs at a much lower scale in the overmodulated case, indicating the larger magnitude of the 200 Hz component at those scales. When examining real signals, overmodulations may occur in the signal and should be taken into consideration.

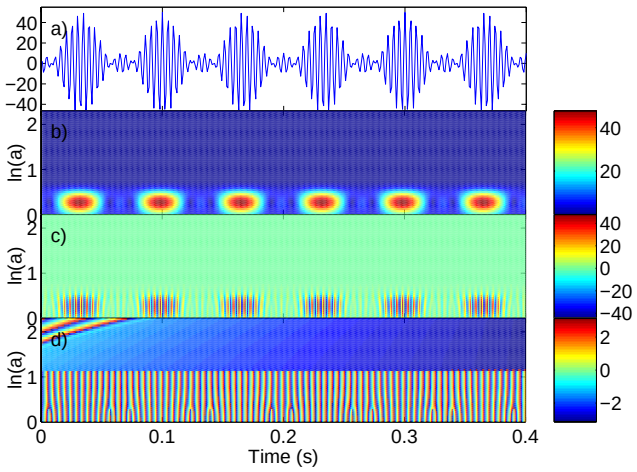

Figure 2.11: Wavelet coefficients for the signal given by $g_a(t) = [20 + 30cos(2\pi 15t)]cos(2\pi 215t)$. Part a) the original signal, $g_a(t)$ Part b) the magnitude of the wavelet coefficients. Part c) the real part of the wavelet coefficients. Part d) the phase of the wavelet coefficients

2.2.3 Frequency Modulation

A frequency-modulated signal is written as

$$g_f(t) = Acos(2\pi f_g t + Pcos(2\pi \nu t)) \tag{2.38}$$

Frequency modulation is inherently a more complicated phenomenon than amplitude modulation. However, it can be analyzed in a similar manner. Equation 2.38 can be rewritten as

$$g_f(t) = Acos(2\pi f_g t)cos(Pcos(2\pi \nu t) - Asin(2\pi f_g t)sin(Pcos(2\pi \nu t)) \tag{2.39}$$

When P is small, this equation can be rewritten

$$g_f(t) = Acos(2\pi f_g t) - APsin(2\pi f_g t)cos(2\pi \nu t)) \tag{2.40}$$

and finally in a form similar to that of the amplitude modulated signal, i.e.

$$g_f(t) = Acos(2\pi f_g t) - \frac{AP}{2}[sin(2\pi[f_g - \nu]t) + sin(2\pi[f_g + \nu]t)] \tag{2.41}$$

The magnitude of the modulating component is attenuated by the wavelet as it was in the case of amplitude modulation. Thus, the wavelet transform of this signal is

$$W[g_f(t)] = Ae^{2\pi f_g t} + \frac{AP_W}{2}[e^{i2\pi[f_g - \nu]t} + e^{i2\pi[f_g + \nu]t}] \tag{2.42}$$

where

$$P_W = \xi(\nu, f_p)P \tag{2.43}$$

Figure 2.12 shows the results from wavelet analysis of a signal given by equation 2.42, with the parameters f_0, ν, P and A set respectively to 215 Hz, 15 Hz, .1 and 20. Part a shows the original signal. Part b shows the amplitude modulation, part c shows the frequency modulation and part d shows the phase modulation. The recovered amplitude modulation is almost constant. The recovered phase amplitude given by $P_W = \xi(15, 215)P$, which is equal to .0928 radians. The level of frequency modulation is $P_W\nu = 1.392$ Hz.

The normalized spectra of the signal given by equation 2.42 and parameters given above are shown in figure 2.13. The Fourier spectrum of the signal is shown in part a. The amplitude, frequency and phase spectra are shown in parts b, c and d, respectively. There is a small amplitude modulation component introduced by the phase modulation at 2ν. The frequency modulation spectra has a peak of magnitude $P\nu$ at the modulation frequency ν. The phase modulation spectra has a peak of magnitude P at the modulation frequency ν.

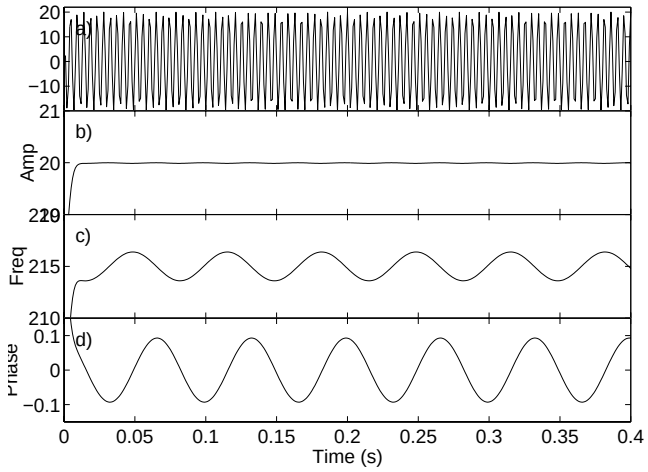

Figure 2.12: Example of signal recovery for $g_f(t) = 20cos[2\pi 215t + .1cos(2\pi 15t)]$, from the scale with peak frequency, $f_p = 215$. Part a) the original signal, $g_f(t)$. Part b) the recovered instantaneous magnitude. Part c) the recovered instantaneous frequency. Part d) the recovered phase lag

The wavelet coefficients over a range of scales are shown in figure 2.14. The level of phase modulation present in the given signal is very small. The difference between the phase of the wavelet coefficients of this signal and the amplitude modulated one, shown in figure 2.8, is most visible at the scales near ln(a) = 1, where the carrier frequencies have been filtered out.

The frequency modulation discussed above is approximate and the derivation of the frequency spectrum of the wide band frequency modulation case is beyond the scope of this work. However, we will use the results derived by Schwartz (1990) to derive analytical expressions

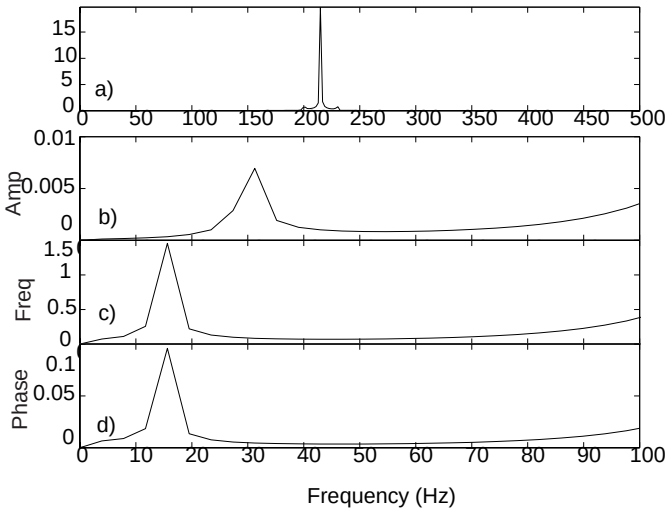

Figure 2.13: Spectra of the modulation of $g_f(t) = 20cos[2\pi 215t) + .1cos(2\pi 15t)]$, from the scale with a peak frequency, $f_p = 215$. Part a) Spectrum of the original signal. Part b) Normalized spectrum of the amplitude modulation. Part c) Normalized spectrum of the frequency modulation. Part d) Normalized spectrum of the phase modulation.

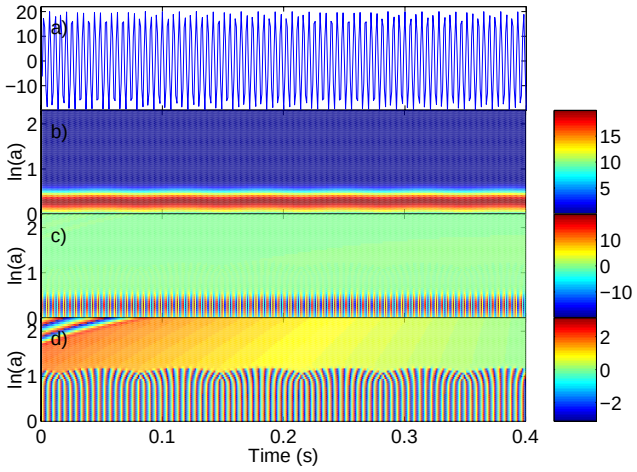

Figure 2.14: Wavelet coefficients for the signal given by $g_f(t) = 20cos[2\pi 215t)+.1cos(2\pi 15t)]$. Part a) The original signal, $g_f(t)$. Part b) Magnitude of the wavelet cofficients. Part c) Real part of wavelet coefficients. Part d) Phase of wavelet coefficients

for the Morlet transform of a wide band case. Equation 2.42, can be written

$$g_f(t) = AJ_0(P)cos(2\pi f_g t) + \sum_{k=1}^{N}(-1)^k AJ_k(P)[sin(2\pi(f_g - k\nu)t) + (-1)^k sin(2\pi(f_g + k\nu)t)] \tag{2.44}$$

The odd harmonics of the modulation are in phase quadrature with the carrier and appear in the phase modulation. The even harmonics of the modulation are in phase with the carrier and appear as part of the amplitude modulation. The Wavelet Transform of the function given in 2.44 is

$$W[g_f(t)] = AJ_0(P)e^{i2\pi f_g t} + \sum_{k=1}^{N}(-1)^k AJ_k(P)i\xi(\nu, f_p)[e^{i2\pi(f_g - k\nu)t} + (-1)^k e^{i2\pi(f_g + k\nu)t}] \tag{2.45}$$

This equation predicts an infinite number of side bands at the phase modulation frequency.

Figure 2.15 shows the signal $g_f(t) = 20cos(2\pi 215t) + \pi cos(2\pi 15t)$. Part a shows the original signal, part b shows the amplitude modulation, part c shows the frequency modulation and part d shows the phase modulation. Note that the amplitude appears to be modulated at twice the frequency of the phase modulation frequency. Figure 2.16 shows the normalized power spectrum of the signal shown in figure 2.12. The spectrum magnitude for frequency modulation is approximately $P\nu$ as was derived in the narrow band case. The phase magnitude is approximately equal to π, which is the value of P in this example. Figure 2.17 shows the wavelet coefficients for several scales. One can see a sinusoidal band of constant magnitude in part b. The fact that the maximum magnitude at time τ appears in a sinusoidally varying range of scales is typical of a wide band modulated signal.

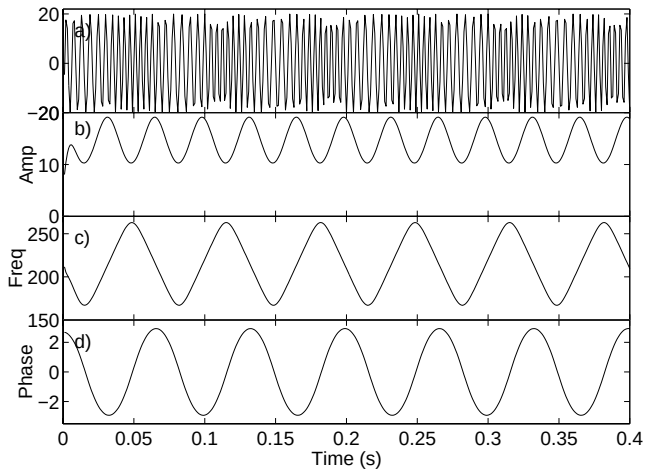

Figure 2.15: Example of signal recovery for $g_f(t) = 20cos(2\pi 215t + \pi cos(2\pi 15t))$, from the scale with peak frequency, $f_p = 215$. Part a) the original signal, $g_f(t)$. Part b) the amplitude modulation. Part c) the frequency modulation Part d) the phase modulation.

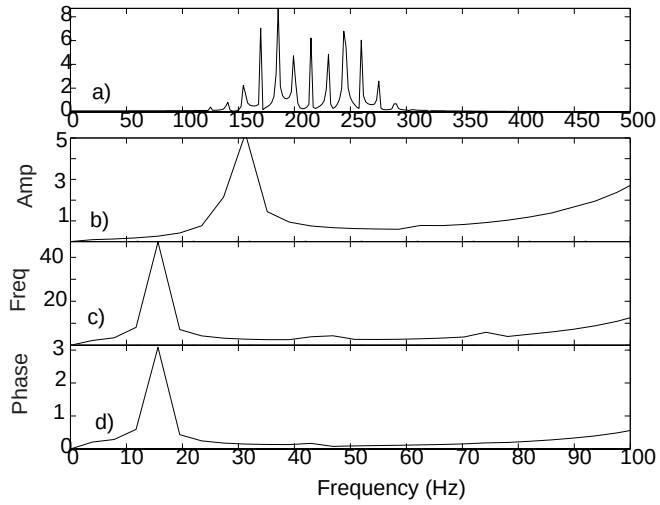

Figure 2.16: Spectra of the modulation of $g_f(t) = 20cos(2\pi 215t) + \pi cos(2\pi 15t)$, from the scale with peak frequency, $f_p = 215$. Part a) Normalized spectrum of the original signal $g_f(t)$. Part b) Normalized spectrum of the amplitude modulation. Part c) Normalized spectrum of the frequency modulation. Part d) Normalized spectrum of the phase modulation.

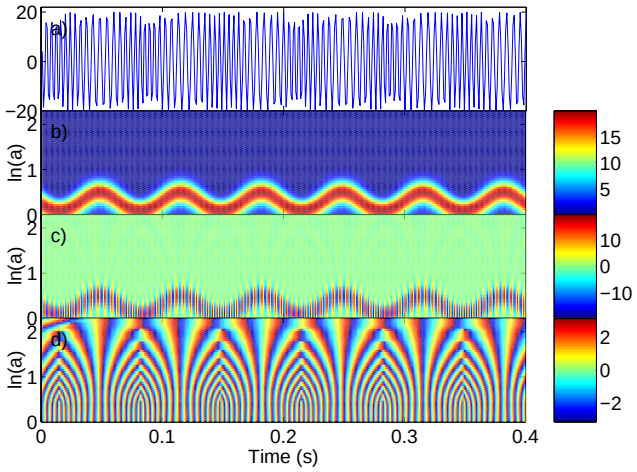

Figure 2.17: Wavelet coefficients for the signal given by $g_f(t) = 20cos(2\pi 215t) + \pi cos(2\pi 15t)$, Part a) the original signal, $g_f(t)$. Part b) Magnitude of the wavelet coefficients. Part c) Real part of the wavelet coefficients. Part d) Phase of the wavelet coefficients.

2.2.4 Unit Impulse

A final example is given to help characterize the wavelet transform to discontinuities. The signal considered is a unit impulse, i.e. the discrete delta function, which is given by

$$g_f(t) = delta(t - t_0) = 1 \qquad t = t_0 \tag{2.46}$$

$$g_f(t) = delta(t - t_0) = 0 \qquad t \neq t_0 \tag{2.47}$$

The convolution of the delta function is most easily evaluated in the time domain using equation 2.1. The result is simply the family of wavelets centered at $t = t_0$. Figure 2.18 shows the wavelet transform of the delta function at a scale with a peak frequency of 215 Hz. The delta function is shown in part a, and the amplitude, frequency and phase of the wavelet coefficients are given in parts b, c and d. The amplitude is a Gaussian curve with its center

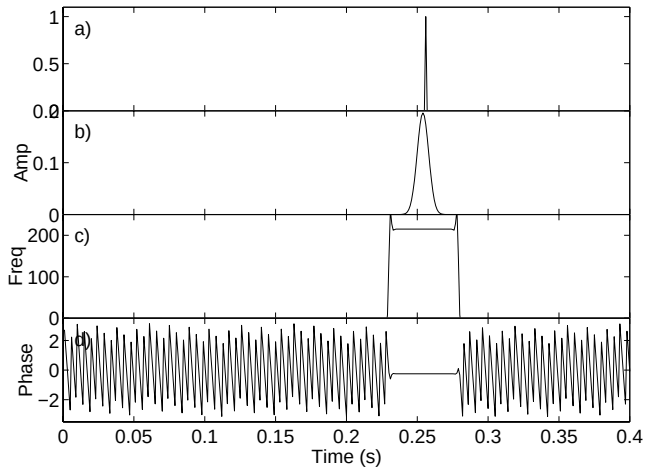

Figure 2.18: Example of signal recovery for $g_f(t) = \delta(t - 0.156)$, from the scale with peak frequency, $f_p = 215$. Part a) the original signal $g_f(t)$. Part b) the recovered instantaneous magnitude. Part c) the recovered instantaneous frequency. Part d) the recovered phase lag.

at $t = t_0$. The frequency approaches zero at times far from $t = t_0$, but is approximately 215 for times given by $t \pm t_s$, where t_s is the support time. The phase lag is constant during the same time. The time variations in the phase lag at the times when instantaneous frequency is zero, are a result of subtracting the carrier from the signal.

Figure 2.19 shows the same signal at a scale that has a peak frequency of 107.5 Hz. The signal is shown in part a, and the amplitude, frequency and phase modulations are shown in parts b, c and d. The amplitude is once again a Gaussian curve, but the temporal support is larger and the maximum amplitude is smaller. The instantaneous frequency is 107.5 Hz for a time larger than that observed in the 215 Hz case, which corresponds to the larger temporal support of the wavelet at this scale.

Figure 2.20 shows the same signal plotted over a range of scales. The signal is shown in

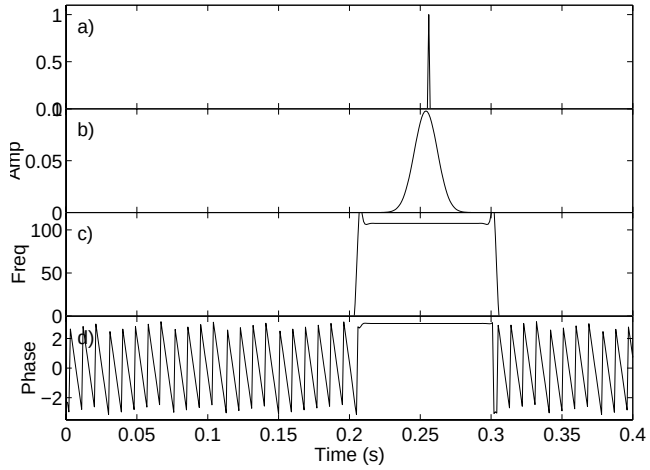

Figure 2.19: Example of signal recovery for $g_f(t) = \delta(t - 0.156)$, from the scale with peak frequency, $f_p = 107.5$. Part a) the original signal, $g_f(t)$. Part b) the recovered instantaneous magnitude. Part c) the recovered instantaneous frequency. Part d) the recovered phase lag.

part a, and the magnitude, real part and phase of the wavelet coefficients are plotted in parts b, c and d respectively. This plot illustrates the same trends discussed above, i.e. that an increase in the temporal support and a decrease in the magnitude of the wavelet accompanies an increase in the scale parameter, a. We also note that smaller magnitude effects are visible in the real part simply because of the contrast between the colors associated with the positive and negative numbers. The similarity between the patterns observed in phase and the alternating negative (blue) and positive (yellow) is obvious. We note that because phase is independent of magnitude, oscillations are detectable in the phase outside of the temporal support.

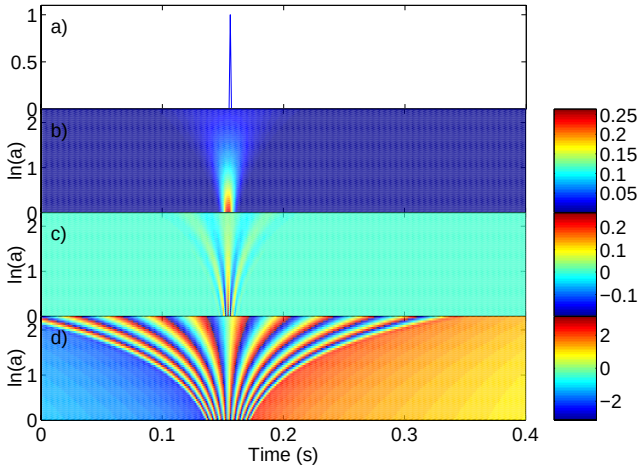

Figure 2.20: Wavelet coefficients for the signal given by $g_f(t) = \delta(t - 0.156)$. Part a) the original signal, $g_f(t)$. Part b) Magnitude of the wavelet coefficients. Part c) Real part of the wavelet coefficients. Part d) Phase of the wavelet coefficients.

Chapter 3

Stability of Shear Flows

In this chapter, we discuss hydrodynamic linear stability theory, and present analyses for the stability of steady and unsteady shear flows. In particular, it is shown that sinusoidal low-frequency mean flow unsteadiness produces amplitude and phase modulations of the most unstable modes. In doing so, we use standard notation such as Ψ and ϕ for the stream function and normal mode representations. We also use τ to denote a stretched time variable. The use of this notation in this chapter should not be confused with its use in other chapters.

3.1 Linear Stability Theory

The field of hydrodynamic stability deals with the subject of prediction and possible control of the transition to turbulence of fluid flows. These issues are important since, in some cases, it may be desirable to produce turbulence to prevent separation or to enhance mixing. In

other cases, it may be desirable to delay the onset of transition to reduce heat transfer rates and drag forces. The linear stability theory describes the first step in a series of instabilities that lead to the breakdown to turbulence. Prediction and description of transition is beyond the scope of linear stability theory. Yet, there is no doubt that linear stability theory is important. It correctly describes the onset and evolution of infinitesimal perturbations. It gives an indication of the relative stability of the flows of interest and it serves as a starting point for weakly nonlinear studies. In relation to this work, we will also establish the experimental background for the effects of mean flow unsteadiness on transition. This will be established by relating results from wavelets to analytical arguments based on linear stability theory.

In linear stability analysis, the approach of normal modes is usually used. In this approach, a perturbation which is proportional to $e^{i\alpha(x-ct)}$ is added to the basic flow $\bar{U}(y)$. For temporal analysis, the wavenumber, α is real and the frequency, αc is complex. The real part of c, c_r, is the phase speed of the wave-like perturbation. The product of the imaginary part of c, c_i, and the wavenumber, α, αc_i, is the growth rate. Thus, if αc_i is positive the disturbance is unstable and will grow exponentially.

3.1.1 Stability of Shear Flows

The vorticity equation for two-dimensional flows is given by

$$\nabla^2\Psi_t + \Psi_y\nabla^2\Psi_x - \Psi_x\nabla^2\Psi_y = \frac{1}{Re}\nabla^4\Psi \tag{3.1}$$

Where Ψ indicates the stream function. In the normal mode approach, the total stream function is expressed as the sum of the basic flow and a perturbation.

$$\Psi = \bar{\Psi} + \epsilon\hat{\Psi} \tag{3.2}$$

By applying this decomposistion, taking the inviscid limit and for small disturbances where nonlinear terms can be neglected, equation 3.1 can be written as

$$\nabla^2\hat{\Psi}_t + \hat{\Psi}_y\nabla^2\bar{\Psi}_x + \bar{\Psi}_y\nabla^2\hat{\Psi}_x - \hat{\Psi}_x\nabla^2\bar{\Psi}_y - \bar{\Psi}_x\nabla^2\hat{\Psi}_y = 0 \tag{3.3}$$

Upon substitution of a basic flow given by $\bar{\Psi}_y = \bar{U}(y)$, the linearized inviscid differential equation for a two-dimensional flow is written as

$$\nabla^2\hat{\Psi}_t + U(y)\nabla^2\hat{\Psi}_x - \bar{U}''(y)\hat{\Psi}_x = 0 \tag{3.4}$$

For a wave-like perturbation of the form

$$\hat{\Psi}(x, y, t) = \phi(y)e^{i\alpha(x-ct)}, \tag{3.5}$$

the Rayleigh equation can then be derived as

$$(-\alpha^2\phi + \phi'') - \phi\frac{\bar{U}''}{\bar{U} - c} = 0 \tag{3.6}$$

Based on this equation, it can then be shown that a necessary condition for inviscid linear instability is that U'' changes sign. The mixing layer profile has an inflection point and is thus unstable.

3.1.2 Stability of Unsteady Shear Flows

Hajj (1997) extended the analysis presented by Shen(1961) for stability of unsteady basic flows. Shen (1961) showed that for special unsteady basic states, where the steady profile is modified by a temporal function, the solution of the stability problem in the inviscid limit, can be reduced to that of the steady flow by transformation of the time variable. In his analysis, Hajj (1997) considered unsteady flows where the velocity profile can be written as

$$U(y,t) = U(y)[1 + \epsilon e^{i\omega_m t}] \tag{3.7}$$

where ω_m represents the frequency of the unsteadiness and ϵ is used to denote small amplitude. By stretching the time variable, a new time scale τ can be defines as

$$\tau = \frac{1}{i\omega_m}\int_0^t (1 + \epsilon e^{i\omega_m t}) d(i\omega_m t) = t + \frac{\epsilon}{i\omega_m}(1 - e^{i\omega_m t}). \tag{3.8}$$

Based on this definition, the time derivative $\partial/\partial t$ can be replaced by $(1 + \epsilon e^{i\omega_m t})\partial/\partial\tau$. The inviscid linearized differential equation governing two-dimensional stream function would then satisfy

$$\nabla^2\Psi_\tau + U(y)\nabla^2\Psi_x - \bar{U}''(y)\Psi_x = 0 \tag{3.9}$$

which is identical to equation 3.4, for steady flow, only with a stretched time scale, τ instead of t. Consequently, equation 3.10 admits solutions of the form

$$\Psi = \phi(y)e^{i\alpha(x-c\tau)} \tag{3.10}$$

as in equation 3.4, only with the modified time function. Using equation 3.10 and substituting for τ, the following expression for Ψ as a function of t is obtained:

$$\Psi = \phi(y)e^{(\alpha c_i t + Acos(\omega_m t+\theta))}e^{i(\alpha(x-c_r t)+Asin(\omega_m t+\theta))}e^{-Acos\theta}e^{-iAsin\theta}, \tag{3.11}$$

where A is equal to $(\alpha\epsilon/\omega_m)\sqrt{c_i^2 + c_r^2}$ and θ is equal to $tan^{-1}c_i/c_r$. The first exponential term governs the amplitude behavior of the instability mode. The periodic portion of that term, $Acos(\omega_m t + \theta)$, represents a modulation of the phase of the instability mode. The last two terms represent a constant phase shift that may be absorbed in the phase of $\phi(y)$. Based on this analysis, the mean flow unsteadiness introduces phase and amplitude modulations at the unsteady frequency in the unstable modes. The contribution of this work is to use wavelets to get amplitude and phase modulations and verify the above arguments. The flows to be used are mixing layers under steady and unsteady basic flow conditions. In addition, the analysis is extended to several stages of transition leading up to turbulence. Although linear theory only covers the earliest stages of transition, it is likely that the study of modulation will be informative throughout the transition process.

3.2 Experimental Setup

The data analyzed in this thesis was taken in a low-turbulence open-return wind tunnel. The mixing layer was formed by the merging of two laminar streams. The upper and lower stream velocities were 7.17 m/s and 1.51 m/s, respectively. This resulted in a velocity ratio $R = (U_1 - U_2)/(U_1 + U_2) = 0.65$. The frequency of the dominant instability mode, f_f, is 215

Hz and its streamwise wavelength, λ_0, is 1.98 cm. More details about the wind tunnel and procedures are given by Hajj et al(1992,1993) and Hajj (1997). The test section is isolated from the pump noise by a sonic throat. This arrangement provided an extremely quiet test section. The free-stream turbulence intensity is $0.0004U_1$ in the high-speed stream and $0.0008U_1$ in the low-speed stream. This background turbulence is distributed over a broad range of frequency components. Such low levels of turbulence intensity are essential for the isolation of the effects of mean flow unsteadiness.

The generation of the sinusoidal mean flow unsteadiness simultaneously in both streams was accomplished by varying the cross sectional area of the sonic throat of the tunnel. A description of the sonic throat modulator used to produce these variations and its effects on the mean flow are given in Hajj (1997). The analysis of free stream velocity fluctuations by Hajj(1997) shows that the low frequency velocity variations, when unsteadiness is imposed are sinusoidal with an amplitude that is two orders of magnitude larger than the background noise of the tunnel. More specifically, the rms level of mean flow unsteadiness is about 3% at a modulation frequency of 35 Hz and showed a distinct sinusoidal character. The velocity fluctuations were obtained using a hot-wire anemometry system. The hot-wire signals were DC and anti-alias filtered and were sampled at 1000 Hz. For the cases discussed in chapter 4, no acoustic forcing was used.

In the acoustically forced mixing layer experiments discussed in chapter 5, both the fundamental and subharmonic components were excited. The excitation system included a function generator controlled by an IBM-PC, a stereo amplifier, and two speakers. This

setup permitted control of the relative phases and amplitudes of the fundamental and the subharmonic. Two different cases of phase controlled excitations were studied. In one case, the phase of the subharmonic was set at zero while the phase of the fundamental was set at $\frac{\pi}{2}$. In the second case, the phase of the subharmonic was set at zero while that of the fundamental was set at $\frac{3\pi}{2}$. The measured amplitudes of the fundamental and the subharmonic modes in the free stream at x = .2 cm were of the order of $0.00014U_1$. The amplitudes of the fundamental components along maximum u'_{rms} in the two excitation cases at x = 0.2 cm were of the order of $0.0018U_1$. The amplitudes of the subharmonic were of the order of $0.0034U_1$. These values are about five times larger than the corresponding values under natural conditions.

Chapter 4

Wavelet Analysis and Modulations of Steady and Unsteady Mixing Layers

In this chapter, wavelet analysis is performed on velocity fluctuations in transitioning steady and unsteady mixing layers to determine the extent of low-frequency modulations and the role of low-frequency mean flow unsteadiness in enhancing these modulations. First, the wavelet coefficients are plotted for all scales. Second, the real part of the wavelet coefficients at the scales corresponding to the fundamental and subharmonic modes are shown to illustrate time variations of these modes. The magnitude and phase of the wavelet coefficients are used to get amplitude, frequency and phase modulations. Normalized spectra of these modulations are presented. Modulation indices are calculated from the wavelet coefficients and their variations with downstream distance are determined.

4.1 Steady Mean Flow

The wavelet analysis of the velocity fluctuation records is performed to determine the time varying characteristics of the steady flow in terms of amplitude and phase modulations. The modulation characteristics of the steady case provide a baseline for determining the effects of mean flow unsteadiness in terms of enhanced low-frequency variations of the unstable modes as explained in chapter 3.

Hajj *et al.* (1992) identified four basic regions for the fundamental and subharmonic development in the early stages of the transition of a mixing layer. The first is the linear instability region where the unstable modes grow exponentially with downstream distance, x. In the second region, the fundamental mode grows at a rate less than that predicted by the linear theory and eventually equilibrates. The growth of the subharmonic component is also affected. The third region is a secondary instability region where the subharmonic undergoes enhanced growth before it saturates. Beyond the third region is a domain where the energy content of both the fundamental and the subharmonic modes start to decrease slightly. In this work, we consider four locations given by x = 2.0, 5.0, 8.0 and 12.0 cm that respectively cover these four regions.

4.1.1 Energy Levels of Unstable Modes

The measured time series and the magnitude, real part and phase of the corresponding wavelet coefficients of the velocity fluctuations in steady mean flow conditions at the four

downstream locations, x = 2.0, 5.0, 8.0 and 12.0 cm are shown in figures 4.1, 4.2, 4.3 and 4.4, respectively. Part a in each of these figures shows the normalized velocity fluctuations, $u'/\Delta U$, where $\Delta U = U_1 - U_2$. Part b shows the magnitude of the wavelet coefficients over a range of scales. Part c shows the real part of the wavelet coefficients and part d shows the phase of the wavelet coefficients. In parts b, c, and d, the abscissa is the translation parameter, τ, and the ordinate is the natural logarithm of the scale number, a. Note that the color scale differs for each of these parts.

At x = 2.0 cm, the band indicating large magnitudes for the wavelet coefficients (figure 4.1.b) at the scale given by ln(a) = 1 shows the high level of energy in the subharmonic mode. The band at the scale given by ln(a) = 0.3 corresponds to the fundamental mode. It is obvious that the subharmonic is the most energetic mode and is less intermittent than the fundamental. Additionally, it is clear that the energy levels of all other components are one to two orders of magnitude smaller than those that include the fundamental or the subharmonic. The use of the real part and the phase of the wavelet coefficients as shown in figure 4.1.c and 4.1.d will be discussed later. At x = 5.0 cm, the magnitude of the wavelet coefficients given in figure 4.2b, shows that the amplitude of the fundamental is slightly larger than that of the subharmonic. The location of the center of the fundamental band varies, which indicates slight variations in its frequency. It also appears that amplitude increases in the subharmonic are synchronized with amplitude decreases in the fundamental and vice-versa.

By x = 8.0 cm, the magnitude of wavelet coefficients given in figure 4.3b, shows that the

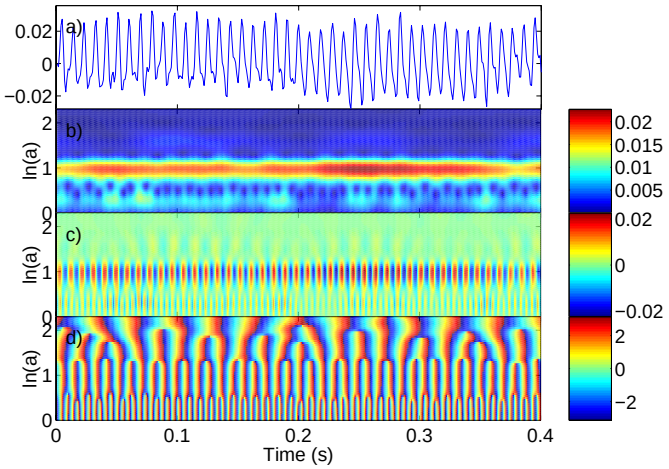

Figure 4.1: Steady Flow at x=2.0 cm a) The fluctuating component of velocity normalized by the velocity deficit b) the magnitude of the wavelet coefficients c) the real part of the wavelet coefficients and d) the phase of the wavelet coefficients

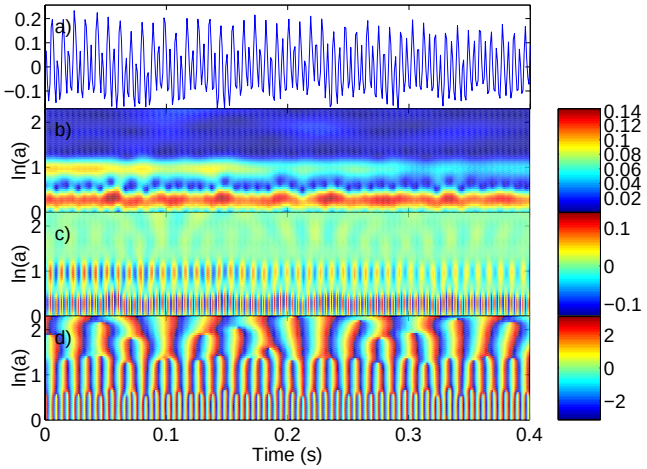

Figure 4.2: Steady Flow at x=5.0 cm a) The fluctuating component of velocity normalized by the velocity deficit b) the magnitude of the wavelet coefficients c) the real part of the wavelet coefficients and d) the phase of the wavelet coefficients

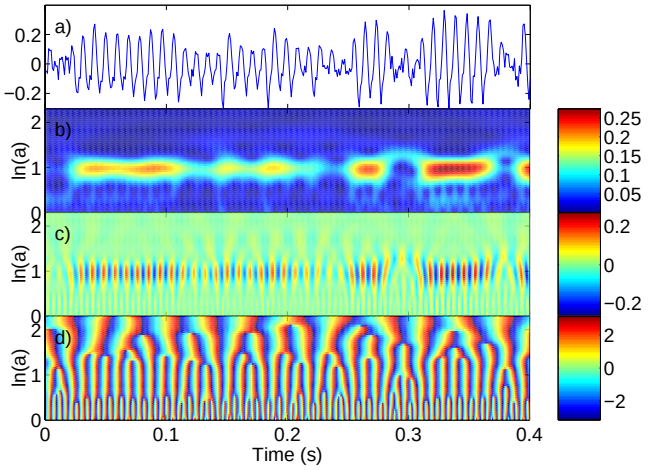

Figure 4.3: Steady Flow at x=8.0 cm a) The fluctuating component of velocity normalized by the velocity deficit b) the magnitude of the wavelet coefficients c) the real part of the wavelet coefficients and d) the phase of the wavelet coefficients

energy of the fundamental has decreased sharply, while that of the subharmonic has grown. The plots also show time intervals where the subharmonic energy is almost gone. Two of these intervals can be clearly identified at t = 0.3 s and t = 0.37 s. Further downstream, at x = 12.0 cm, figure 4.4b shows temporal variations in the amplitudes of both modes. Also, modes other than the fundamental and subharmonic are beginning to gain energy. This is an indication of the energy redistribution which is associated with the breakdown to turbulence.

More details about the fundamental and subharmonic characteristics can be obtained from figures 4.5, 4.6, 4.7, and 4.8, which show the real part of the wavelet coefficients at the scales corresponding to the fundamental and subharmonic modes at x = 2.0, 5.0, 8.0 and 12.0 cm, respectively. Part a in these figures shows the normalized velocity fluctuations. Parts b and

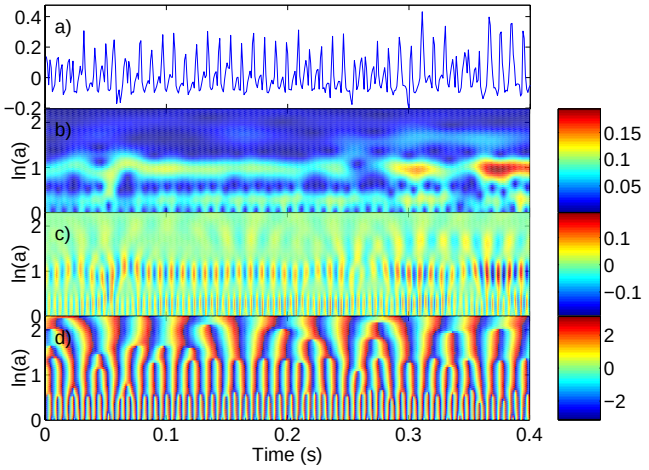

Figure 4.4: Steady Flow at x=12.0 cm a) The fluctuating component of velocity normalized by the velocity deficit b) the magnitude of the wavelet coefficients c) the real part of the wavelet coefficients and d) the phase of the wavelet coefficients

c show the real part of the wavelet coefficients at the scales with peak frequencies equal the fundamental and subharmonic respectively. These parts represent horizontal cross sections of part c of the three dimensional plots (figures 4.1, 4.2, 4.3 and 4.4) at the scale given by ln(a) = 0.3 for the fundamental (f_0 = 215 Hz) and at the scale given by ln(a) = 1 for the subharmonic ($f_0/2$ = 107.5 Hz). At x = 2.0 cm, a comparison of figures 4.5b and 4.5c shows that the amplitude of the subharmonic component is larger than that of the fundamental. This is most likely due to feedback from the vortex merging process. We note also that, while the subharmonic has a more or less constant amplitude, the amplitude of the fundamental shows relatively larger variations. At x = 5.0 cm, parts b and c of figure 4.6 show that the amplitude of the fundamental has undergone a tenfold increase of its value at x=2.0 cm. On the other hand, the amplitude of the subharmonic has increased by about four times of its

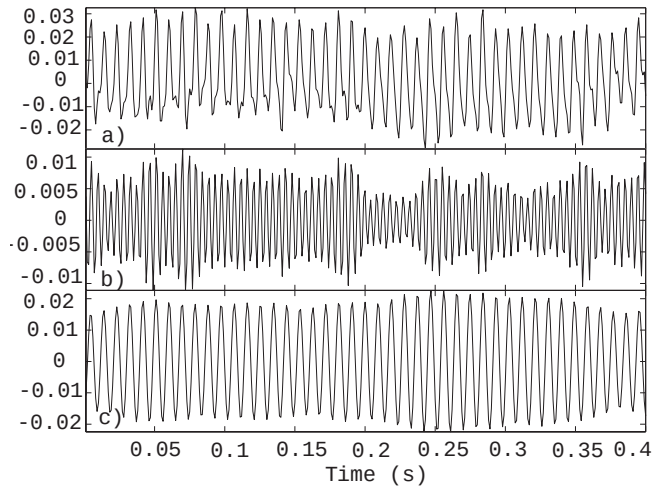

Figure 4.5: Steady Flow at x=2.0 cm a) The fluctuating component of velocity normalized by the velocity deficit b) the fundamental component and c) the subharmonic component

value at x=2.0 cm. The level of variations in the amplitude for both modes is lower at x = 5.0 cm than it was at x = 2.0 cm.

The results for x = 8.0 cm presented in figure 4.7.b and 4.7.c show that the amplitude of the fundamental starts to show significant variations with time. The peak to peak level varies between 0.10 and 0.02. The same level of variation is observed for the subharmonic. Note also that this variation is synchronized between the two modes, i.e. a high-level amplitude of the subharmonic is accompanied by a high level in the fundamental's amplitude and vice-versa. This synchronization is evidence of the parametric interaction between the two modes whereby an enhanced fundamental leads to the growth of the subharmonic. In parts b and c of figure 4.8, at x = 12.0 cm we note a lower level in the variations of the amplitudes of both modes. We also observe that the same type of synchronization noted at x = 8.0 cm is present at this location.

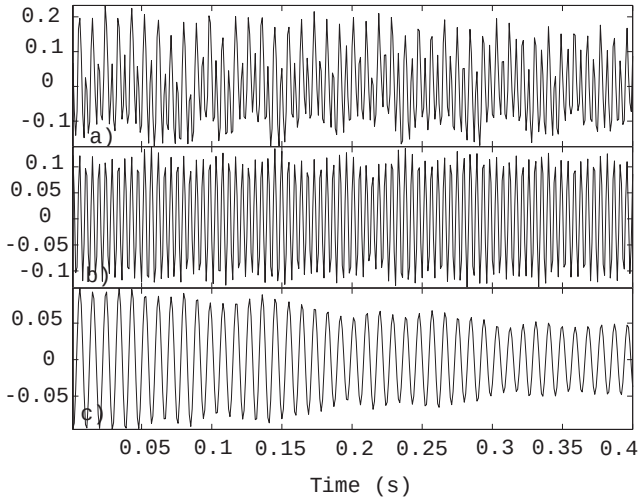

Figure 4.6: Steady Flow at x=5.0 cm a) The fluctuating component of velocity normalized by the velocity deficit b) the fundamental component and c) the subharmonic component

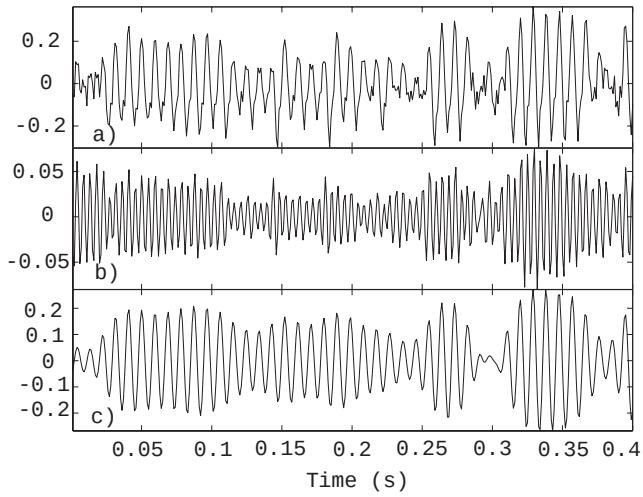

Figure 4.7: Steady Flow at x=8.0 cm a) The fluctuating component of velocity normalized by the velocity deficit b) the fundamental component and c) the subharmonic component

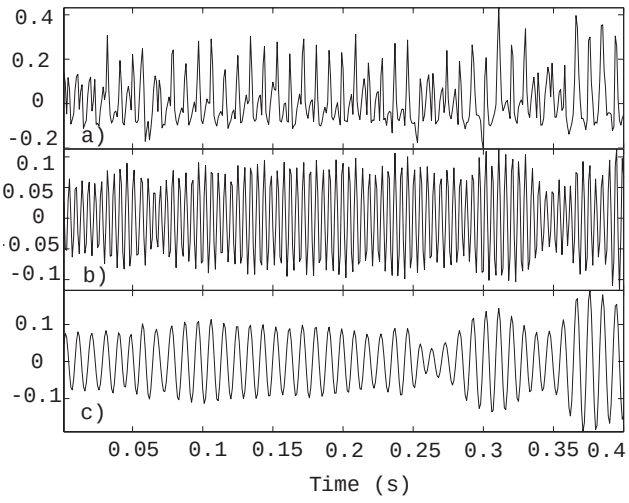

Figure 4.8: Steady Flow at x=12.0 cm a) The fluctuating component of velocity normalized by the velocity deficit b) the fundamental component and c) the subharmonic component

4.1.2 Modulation Characteristics of the Fundamental Mode

In this section, amplitude, frequency and phase modulations of the fundamental in the steady mixing layer are determined from the magnitude and phase of the wavelet coefficients. Figures 4.9, 4.10, 4.11, and 4.12, show these quantities along with the corresponding velocity fluctuations at x = 2.0, 5.0, 8.0 and 12.0 cm, respectively. Part a of these figures shows the normalized velocity fluctuations. Parts b, c, and d show the amplitude modulation, the frequency modulation and the phase modulation, respectively. Since it is by no means certain that the actual carrier will be equal to 215 Hz, the procedure described in chapter 2 for determing an average carrier frequency, $F\bar{M}$, for each signal has been followed. Once the carrier frequency was determined at the scale with peak frequency equal to the fundamental frequency, the carrier was subtracted from the phase of the wavelet coefficients to give the

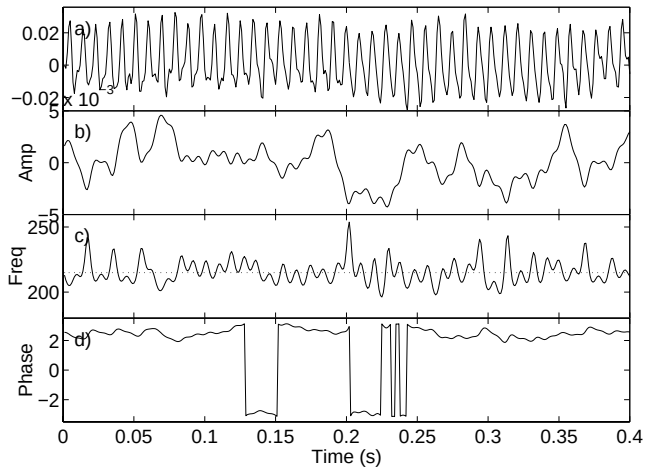

Figure 4.9: Steady Flow: Modulation of the fundamental at x=2.0 cm a) The fluctuating component of velocity normalized by the velocity deficit b) the amplitude modulation c) the frequency modulation and d) the phase modulation

instantaneous phase lag i.e. the phase modulation.

At x = 2.0 cm, the results presented in figure 4.9 show that the amplitude modulation is about one order of magnitude smaller than the amplitude of the signal. The instantaneous frequency varies slightly around 215 Hz. The phase lag shows also small variations. At x = 5.0 cm, the results in figure 4.10.b, show that the level of amplitude modulation of the fundamental component has increased. However, the level of variation in the frequency and phase modulation as shown in figures 4.10.c and 4.10.d remains the same as it was at x = 2.0 cm.

By x = 8.0 cm, the results presented in figure 4.11 show that there are large modulations in the amplitude, frequency and phase of the fundamental. An interesting phenomenon is noted at t = 0.28 s. The amplitude modulation is approximately equal in magnitude to the carrier

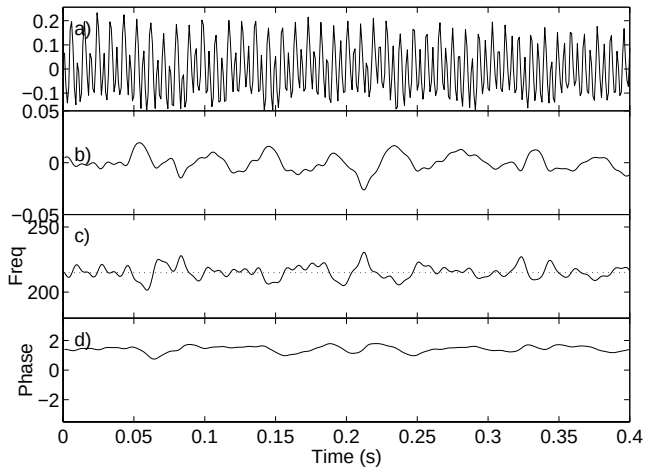

Figure 4.10: Steady Flow: Modulation of the fundamental at x=5.0 cm a) The fluctuating component of velocity normalized by the velocity deficit b) the amplitude modulation c) the frequency modulation and d) the phase modulation

amplitude. Consequently, the phase becomes undefined. The instantaneous frequency shows a sharp decrease due to this discontinuity. Since the frequency spike goes outside the band of frequencies that are passed by the wavelet, it indicates the disappearance of the carrier. Since this phenomenon is characterized by modulation amplitude that exceeds the carrier amplitude, it is referred to as overmodulation. At x = 12.0 cm, the results presented in figure 4.12 show smaller variations in amplitude, frequency and phase than the ones observed at x = 8.0 cm. In particular, the phase appears to steadier, except for a jump in phase near t = 0.36 s. Since the discontinuity in phase corresponds to a time when the amplitude modulation is large and negative, this jump in phase is due to overmodulation.

Figures 4.13, 4.14, 4.15, and 4.16 show the power spectra of the signal and of the amplitude, frequency, and phase modulations at the same downstream locations shown in the time

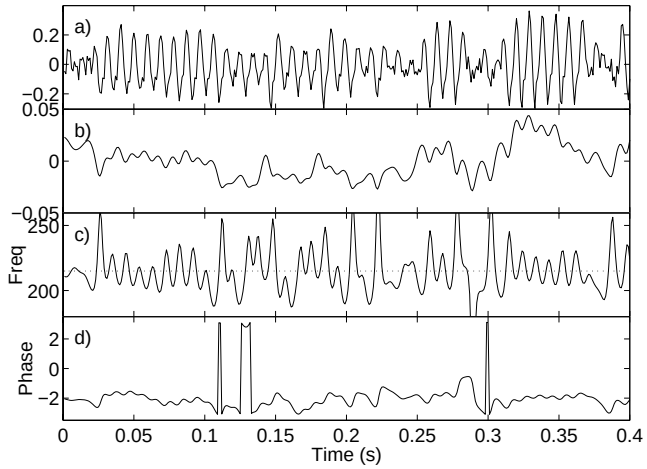

Figure 4.11: Steady Flow: Modulation of the fundamental at x=8.0 cm a) The fluctuating component of velocity normalized by the velocity deficit b) the amplitude modulation c) the frequency modulation and d) the phase modulation

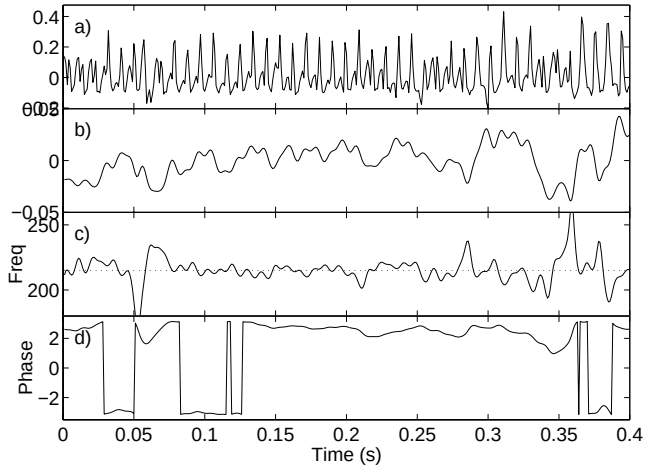

Figure 4.12: Steady Flow: Modulation of the fundamental at x=12.0 cm a) The fluctuating component of velocity normalized by the velocity deficit b) the amplitude modulation c) the frequency modulation and d) the phase modulation

domain. In each case, the magnitude has been multiplied by $\sqrt{2}$ in order to yield the peak values instead of rms values. Furthermore, the spectra of the modulations were normalized by ξ as was done in the examples presented in chapter 2. In order to obtain results that are more accurate, ensemble averages of twenty-four samples are taken at each location. Parts a, b, c and d of each figure show respectively, the power spectra of the time series at each location, the power spectra of the amplitude modulation, the power spectra of the frequency modulation and the power spectra of the phase modulation. There are some inherent sources of error in the calculation of spectra for phase and frequency related to the phenomenon of overmodulation. When the magnitude of the wavelet coefficients becomes zero, the phase is undefined. Practically speaking, whenever the magnitude becomes small, large variations are seen in phase which are not physically significant. These variations manifest as large spikes in the frequency modulation. Jones (1988) suggests that there is no way of removing the errors introduced by overmodulation except to take samples that do not contain overmodulation events. However, given the frequent occurrence of overmodulation events in these data sets, we simply accept them as a source of error. The units of the original signal and the amplitude modulation are identical, nondimensional velocity. The units of the frequency modulation are Hertz and the units of the phase modulation are radians.

In figure 4.13, the velocity spectrum, part a, shows two components at the fundamental and subharmonic frequencies. The subharmonic has a slightly larger amplitude than the fundamental. As observed in the time domain plots, figures 4.9.b-d, the modulation levels are quite small. Yet, we notice the large peak at 28 Hz in the spectra of the amplitude, phase

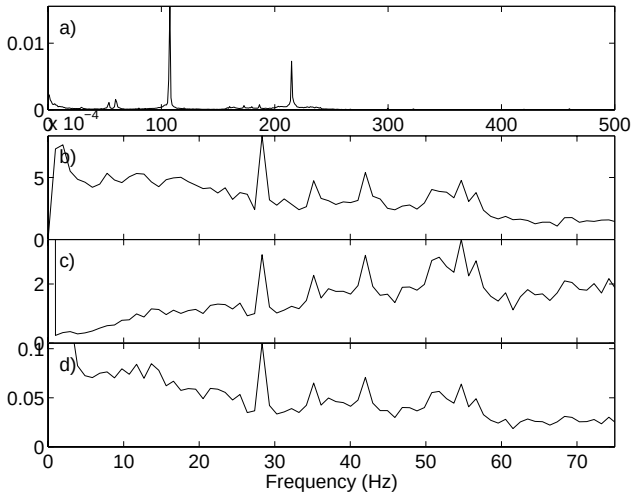

Figure 4.13: Steady Flow: Spectra at x=2.0 cm of a) the fluctuating component of velocity normalized by the velocity deficit b) the amplitude modulation c) the frequency modulation and d) the phase modulation

and frequency modulations. Interestingly enough, the 28 Hz peak roughly corresponds to one eighth the fundamental frequency. Note that peaks are also present at this location at 35 Hz and 42 Hz.

Figure 4.14 shows that the velocity fluctuations at x = 5.0 cm contain the two components at the fundamental and the subharmonic frequencies. No distinctive peaks are noted in the amplitude modulation spectrum, figure 4.14.b, as were noted at x = 2.0 cm. The spectra of the phase and frequency modulations still show peaks at 28 Hz. In figure 4.15, the velocity spectrum at x = 8.0 cm shows that the subharmonic is much larger than the fundamental. The modulation spectra magnitudes are very small. There are not any sharp peaks visible in the spectra at this location, which may be due to redistribution of energy among many spectral components. In figure 4.16, the velocity fluctuation spectrum at x = 12.0 cm,

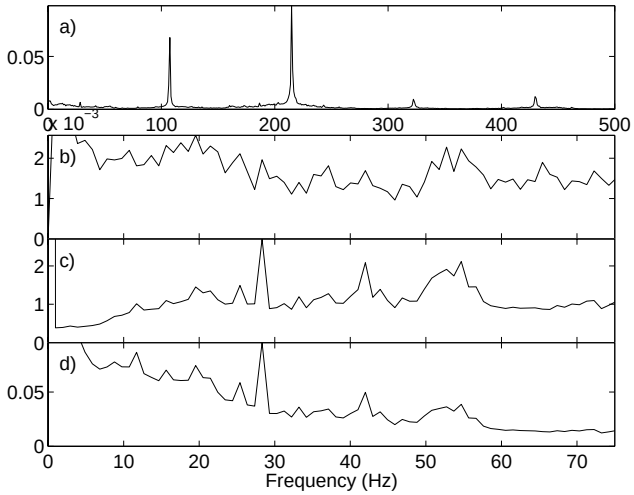

Figure 4.14: Steady Flow: Spectra at x=5.0 cm of a) the fluctuating component of velocity normalized by the velocity deficit b) the amplitude modulation c) the frequency modulation and d) the phase modulation

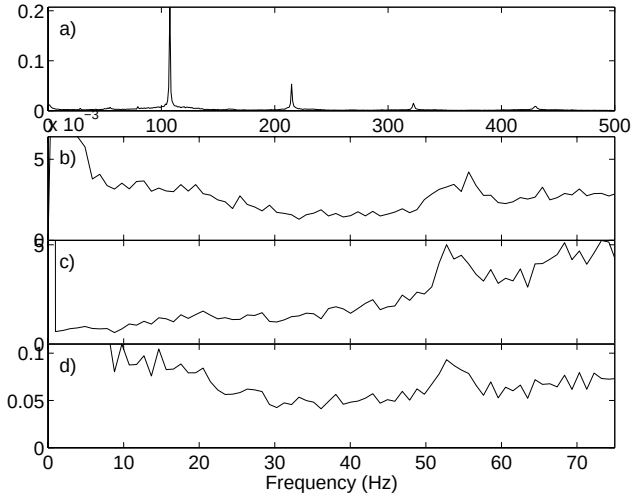

Figure 4.15: Steady Flow: Spectra at x=8.0 cm of a) the fluctuating component of velocity normalized by the velocity deficit b) the amplitude modulation c) the frequency modulation and d) the phase modulation

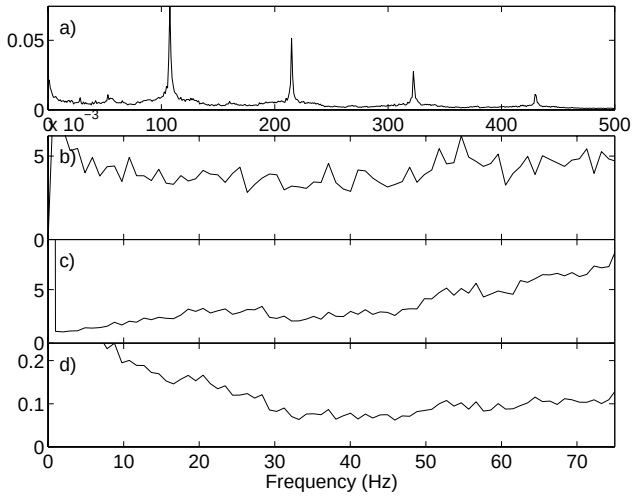

Figure 4.16: Steady Flow: Spectra at x=12.0 cm of a) The fluctuating component of velocity normalized by the velocity deficit b) the amplitude modulation c) the frequency modulation and d) the phase modulation

shows that side bands of the fundamental and subharmonic frequencies have increased in magnitude. Note also that the while no particular peaks are noticeable, the magnitude of the whole range of modulation frequencies has increased. This corresponds to the filling of spectral valleys observed in transitioning flows. The result of this trend is the disappearance of sharp peaks in the spectra and cascade of energy from low-frequency to high-frequency components.

4.2 Unsteady Mean Flow

The data records analyzed in this section are velocity fluctuation measurements taken from mixing layers with low frequency mean flow unsteadiness. The experimental setup has been

described in chapter 3.

4.2.1 Energy Levels of Unstable Modes

Figures 4.17, 4.18, 4.19 and 4.20 show the wavelet coefficients obtained when the unsteady component is introduced in the mean flow. The results shown are for the same downstream locations considered in the steady case, namely, x = 2.0, 5.0, 8.0 and 12.0 cm. Part a of figures 4.17, 4.18, 4.19 and 4.20 shows the normalized velocity fluctuations. Parts b, c and d show respectively, the magnitude, the real part and the phase of the wavelet coefficients. From the outset, it is apparent that mean flow unsteadiness has substantially changed the characteristics of the flow. The time series measurements from the unsteady flow certainly show higher levels of variations.

At x = 2.0 cm, the magnitude of the wavelet coefficients presented in figure 4.17.b shows that there are three modes with high energy levels. The fundamental and subharmonic are present as they were in the steady case at the scales given by ln(a) = 0.3 and ln(a) =1.0, respectively. Additionally, there is band of coefficients with large magnitudes that represents the unsteady component at the scale given by ln(a) = 2.1. The energy level of the unsteady component does not show any time varying characteristics at this location. The subharmonic and fundamental, on the other hand, are more intermittent. By x = 5.0 cm, the results shown in figure 4.18.b show that the fundamental has attained the highest energy level. Moreover, there seem to be significant time variations in the energy level of both the fundamental and

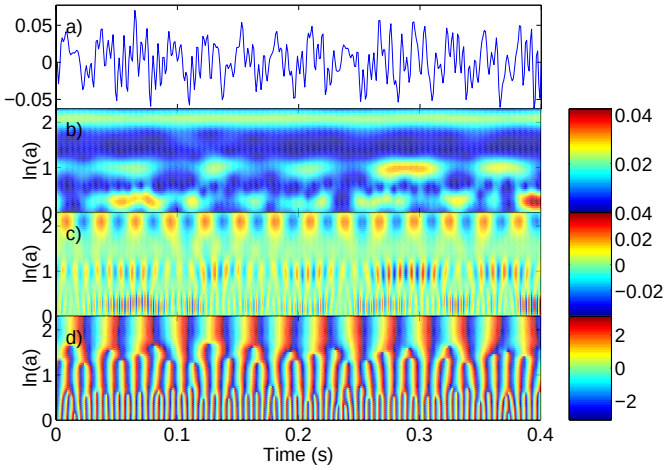

Figure 4.17: Unsteady Flow at x=2.0 cm. a) The fluctuating component of velocity normalized by the velocity deficit b) the magnitude of the wavelet coefficients c) the real part of the wavelet coefficients and d) the phase of the wavelet coefficients

the subharmonic components.

Figure 4.19.b shows the magnitude of the wavelet coefficients at x = 8.0 cm. By this location, the subharmonic is the most energetic mode. As in the steady case, synchronized variations in the magnitude of the wavelet coefficients of the subharmonic and the fundamental components are observed. This indicates the role of the parametric resonance in enhancing the energy level of the subharmonic mode. In comparison to the steady case at this location, the magnitudes of both the fundamental and subharmonic are enhanced. By x = 12.0 cm, the results in figure 4.20 show that the signal has become very intermittent and several modes have significant levels of energy. The subharmonic and fundamental still have high levels of energy, however, they are also highly intermittent. One mode that has gained energy is the scale given by ln(a) = 1.6, which corresponds to the second subharmonic.

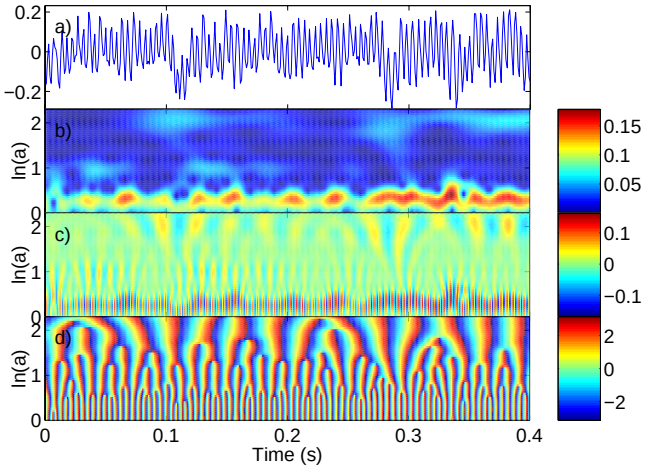

Figure 4.18: Unsteady Flow at x=5.0 cm. a) The fluctuating component of velocity normalized by the velocity deficit b) the magnitude of the wavelet coefficients c) the real part of the wavelet coefficients and d) the phase of the wavelet coefficients

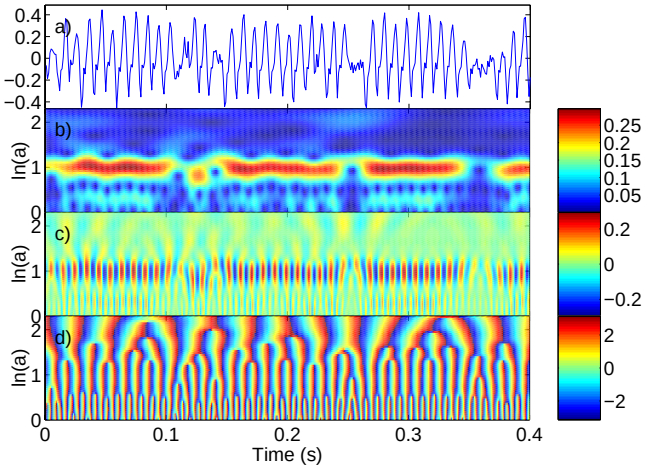

Figure 4.19: Unsteady Flow at x=8.0 cm. a) The fluctuating component of velocity normalized by the velocity deficit b) the magnitude of the wavelet coefficients c) the real part of the wavelet coefficients and d) the phase of the wavelet coefficients

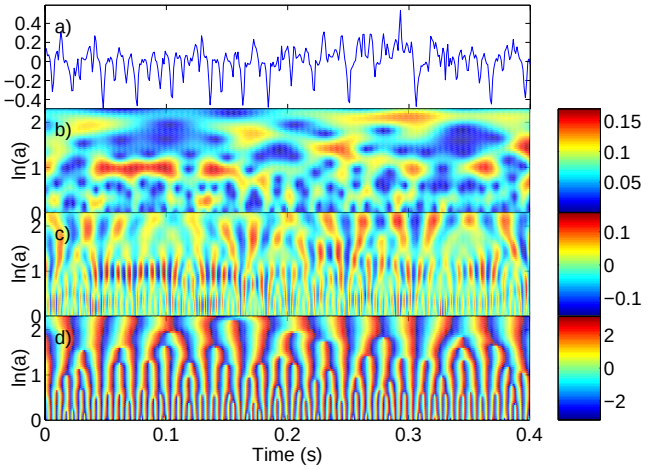

Figure 4.20: Unsteady Flow at x=12.0 cm a) The fluctuating component of velocity normalized by the velocity deficit b) the magnitude of the wavelet coefficients c) the real part of the wavelet coefficients d) the phase of the wavelet coefficients

More information about the time-varying characteristics of the fundamental and the subharmonic components are obtained from the real component of the wavelet coefficients at their respective scales. These components at different downstream locations are shown in figures 4.21, 4.22, 4.23 and 4.24. Part a of these figures shows the velocity fluctuations. The real component of the wavelet coefficients at the scales corresponding to the fundamental and the subharmonic components are shown in parts b and c of the same figures.

In figure 4.21, which shows results at x = 2.0 cm, the fundamental and subharmonic vary considerably in amplitude. The maximum amplitudes of both modes are larger than those observed under steady mean conditions. We also note that the variations are not synchronized. The local maxima in the fundamental in figure 4.21.b at t = 0.12 s and at t = .33 s are not synchronous with any specific features in the subharmonic in figure 4.21.c. This is

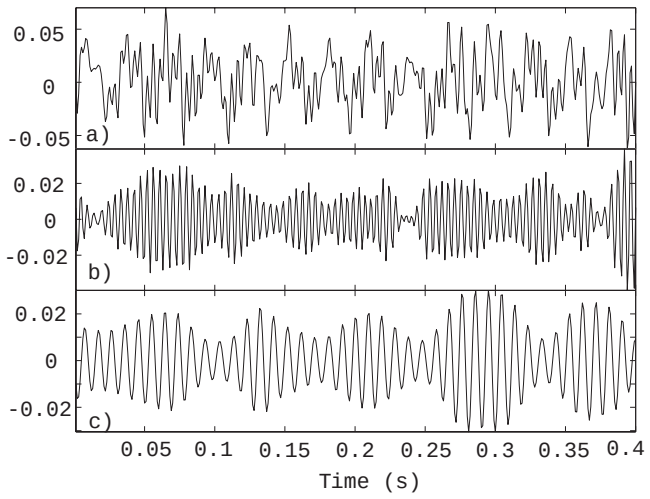

Figure 4.21: Unsteady Flow at x=2.0 cm. a) The fluctuating component of velocity normalized by the velocity deficit b) the fundamental component and c) the subharmonic component

expected since, at this stage, the two modes are growing independently.

By x = 5.0 cm, the results presented in figure 4.22, show intermittent breaks in the time series of the velocity fluctuations. While the fundamental and subharmonic modes have almost the same maximum levels as in the steady case, they certainly show much larger variations. Moreover, by examining these variations, it can be established that the breaks in the velocity fluctuations are associated with large decreases in the amplitude of the subharmonic. It should also be noted that the variations in the fundamental and subharmonic amplitudes are not completely synchronized.

At x = 8.0 cm, the fluctuations shown in figure 4.23, have more definite and periodic breaks. These breaks are related to the subharmonic growth. Note also that the variations of both modes are synchronized at this location. The same observations can be made at x = 12.0

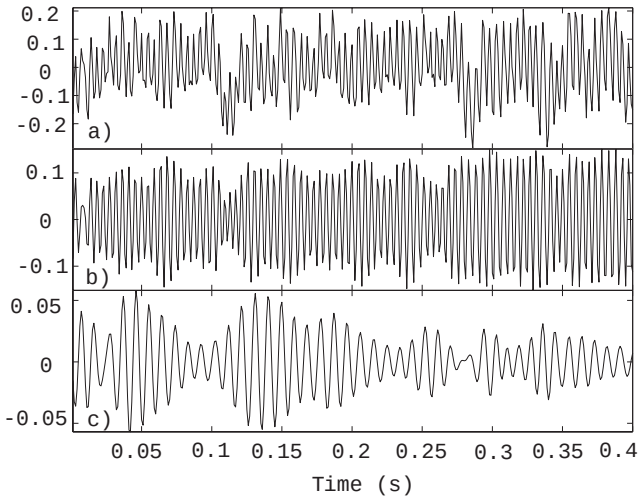

Figure 4.22: Unsteady Flow at x=5.0 cm. a) The fluctuating component of velocity normalized by the velocity deficit b) the fundamental component and c) the subharmonic component

cm from figure 4.24, although the breaks have become less periodic.

4.2.2 Modulation Characteristics of the Fundamental Mode

Amplitude, frequency and phase modulations of the fundamental component are obtained from the wavelet coefficients. As explained in chapter 2, the magnitude of the wavelet coefficients is used to obtain the amplitude modulations at the scale with the peak frequency equal to the fundamental frequency. The phase is used to obtain the frequency and phase modulations. The results are shown in figures 4.25, 4.26, 4.27 and 4.28. In part a of these figures, the velocity record is shown. The amplitude, frequency and phase modulations are shown in parts b, c, and d, respectively. Additionally, a horizontal line representing the nominal value of the carrier is shown in part c. The key features of interest in the time

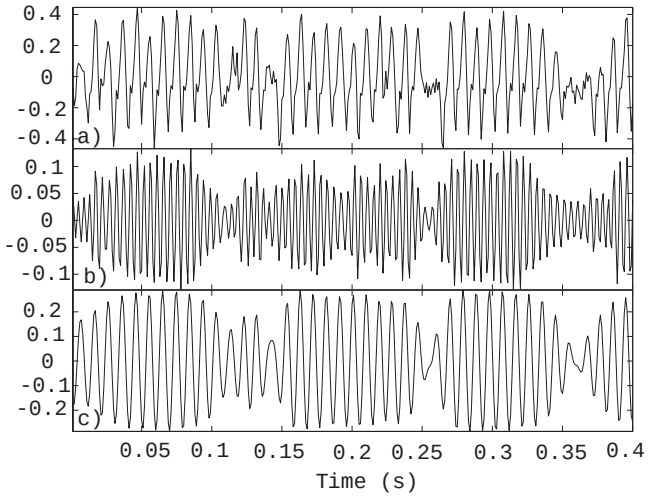

Figure 4.23: Unsteady Flow at x=8.0 cm. a) The fluctuating component of velocity normalized by the velocity deficit b) the fundamental component and c) the subharmonic component

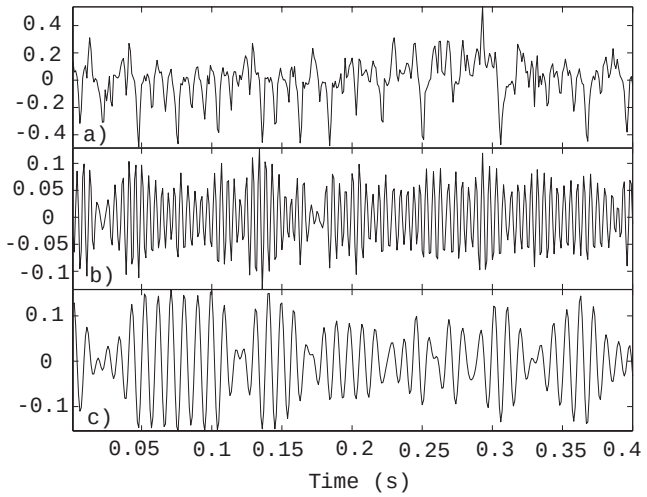

Figure 4.24: Unsteady Flow at x=12.0 cm. a) The fluctuating component of velocity normalized by the velocity deficit b) the fundamental component and c) the subharmonic component

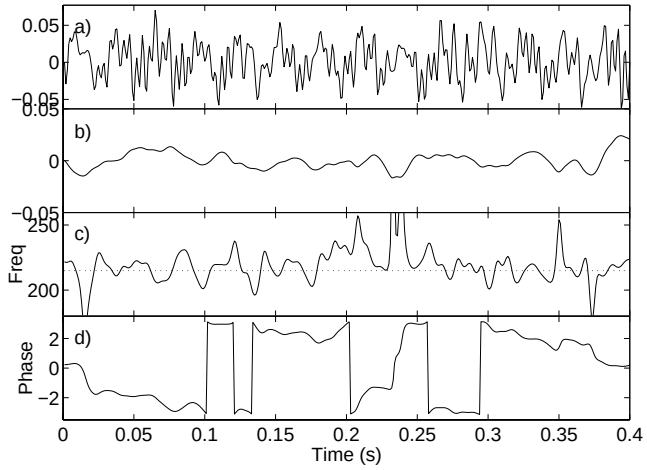

Figure 4.25: Unsteady Flow: Modulation of the fundamental at x=2.0 cm. a) The fluctuating component of velocity normalized by the velocity deficit b) the amplitude modulation c) the frequency modulation and d) the phase modulation

domain plots are the time-varying characteristics. In particular, we note the intermittent changes in the magnitude and overmodulations.

At x = 2.0 cm, figure 4.25 shows that amplitude, frequency and phase of the fundamental are very highly modulated. An overmodulation event takes place near t = 0.23 s. In figure 4.26, at x = 5.0 cm, the level of modulation is higher than in the steady case at the same location. While the amplitude modulation appears fairly stationary, the phase and frequency modulations show large variations. In figure 4.27, at x = 8.0 cm, the most significant observation is the high levels of amplitude, which are interrupted by brief periods of near-zero amplitudes. This type of intermittent behavior is mirrored in the frequency and phase. At times when the amplitude is large, the phase is fairly constant and the frequency modulation has a relatively small range. On the other hand, when the amplitude is relatively small, the

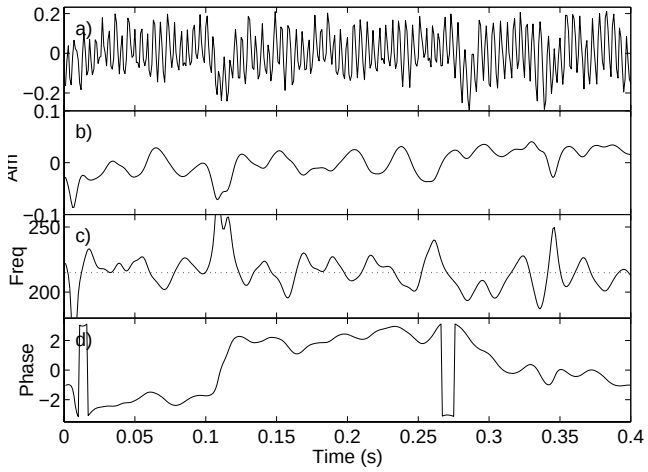

Figure 4.26: Unsteady Flow: Modulation of the fundamental at x=5.0 cm. a) The fluctuating component of velocity normalized by the velocity deficit b) the amplitude modulation c) the frequency modulation and d) the phase modulation

phase changes abruptly and the level of frequency modulation is large.

In figure 4.28, at x = 12.0 cm, overmodulations occur near t = 0.02 s and near t = 0.17 s. Large modulations in the amplitude, frequency and phase occur more frequently at this location than at the other locations. There are peaks in the frequency modulation plot, 4.28.c, which occur at regular intervals. These peaks coincide with the minima of the amplitude modulation, indicating that the amplitude and frequency modulations of the flow are synchronized.

Several nonstationary features occur in the modulations of the unsteady signals. As a result, detection of sharp peaks in the modulation spectra, figures 4.29, 4.30, 4.31 and 4.32, is difficult. The unsteady set of data used to obtain the spectra, like the steady one, consisted of 24 data records of 1024 data points sampled at 1000 Hz. Part a of each of figures 4.29,

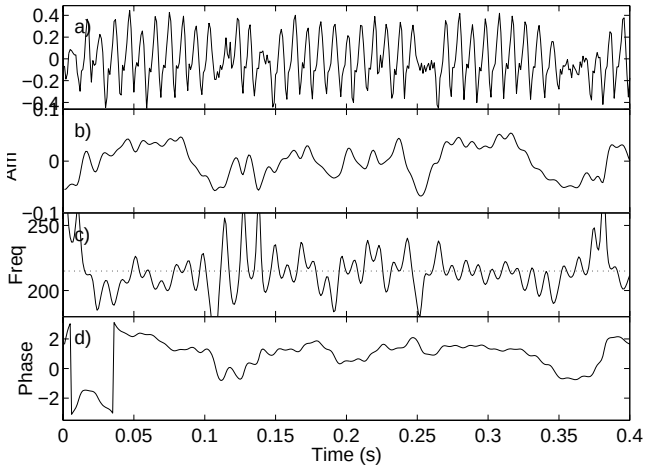

Figure 4.27: Unsteady Flow: Modulation of the fundamental at x=8.0 cm. a) The fluctuating component of velocity normalized by the velocity deficit b) the amplitude modulation c) the frequency modulation and d) the phase modulation

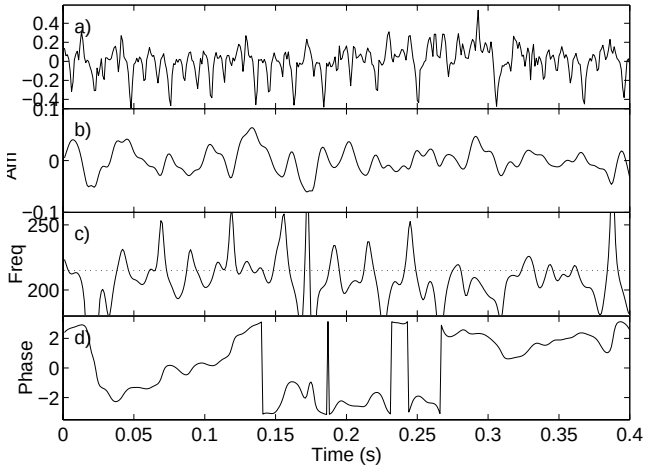

Figure 4.28: Unsteady Flow: Modulation of the fundamental at x=12.0 cm. a) The fluctuating component of velocity normalized by the velocity deficit b) the amplitude modulation c) the frequency modulation and d) the phase modulation

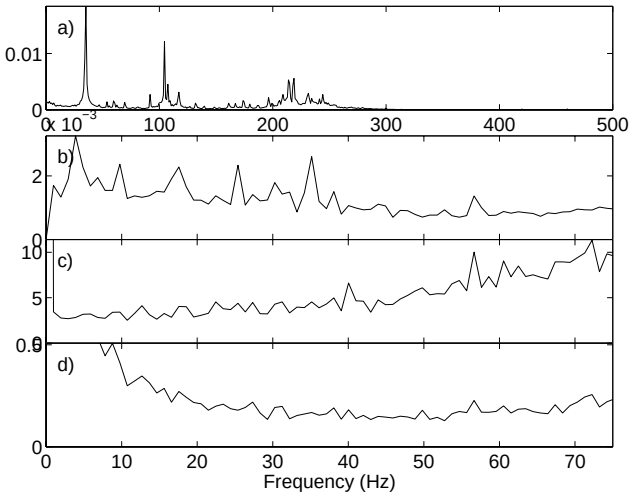

Figure 4.29: Unsteady Flow: Spectra at x=2.0 cm of a) the fluctuating component of velocity normalized by the velocity deficit b) the amplitude modulation c) the frequency modulation and d) the phase modulation

4.30, 4.31 and 4.32 contains the power spectrum of the data series. Part b shows the power spectrum of the amplitude modulations. Part c shows the power spectrum of the frequency modulations and part d shows the power spectrum of the phase modulations.

In figure 4.29, the power spectrum of the velocity fluctuations shows peaks at frequencies corresponding to the fundamental, subharmonic and low frequency unsteadiness modes. As for the modulation spectra, clear and distinct peaks are observed only in the amplitude modulation part of the plot. In particular, we note peaks near 5, 18, 28 and 35 Hz. The spectra of the phase and frequency modulations show characteristics that are more random.

By x = 5.0 cm, figure 4.30.a shows a distinctive peak at the frequency corresponding to the fundamental component. Relatively smaller peaks are observed at the frequencies of the

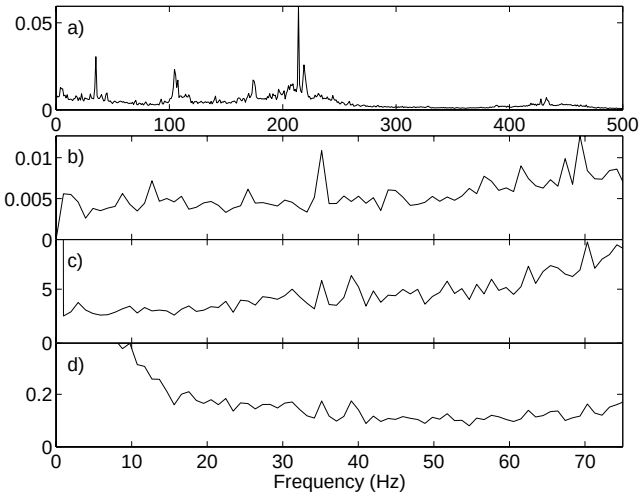

Figure 4.30: Unsteady Flow: Spectra at x=5.0 cm of a) the fluctuating component of velocity normalized by the velocity deficit b) the amplitude modulation c) the frequency modulation and d) the phase modulation

subharmonic and the low-frequency component of the mean flow. Because the fundamental has a larger amplitude than the low-frequency component, it should be easier to detect the modulation phenomenon. Parts b, c, and d of figure 4.30 show peaks at 35 Hz, especially in the amplitude modulation which shows the enhanced modulations of the fundamental by the low-frequency component of the mean flow as predicted by the analysis of Hajj (1997).

At x = 8.0 cm, figure 4.31.a shows the most energetic component is the subharmonic mode. The level of fluctuations at the fundamental component is almost an order of magnitude lower. Two other components are present at 35 Hz and 70 Hz. Figures 4.31.b, c and d do not show specific peaks near 35 Hz, indicating that at this stage of transition, the modulation of the fundamental is more of a random phenomenon. This also may be explained by the fact that the subharmonic is the most energetic mode.

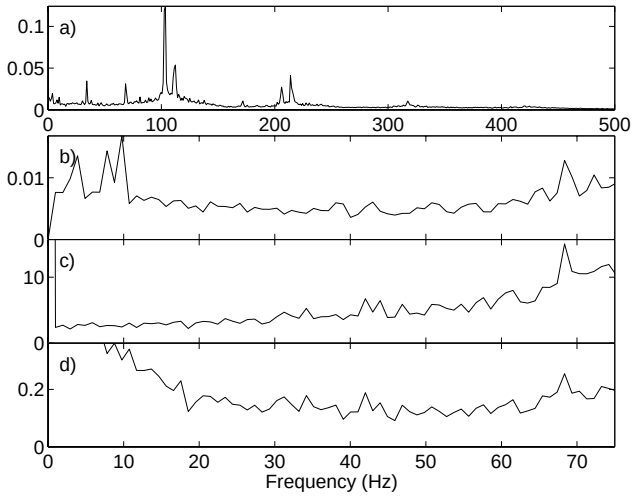

Figure 4.31: Unsteady Flow: Spectra at x=8.0 cm of a) the fluctuating component of velocity normalized by the velocity deficit b) the amplitude modulation c) the frequency modulation and d) the phase modulation

At x = 12.0 cm, the velocity spectrum shows components at the fundamental, subharmonic, mean flow unsteadiness and the second subharmonic. The modulation spectra show peaks at 35 Hz, indicating that the fundamental is modulated in amplitude, frequency and phase by the low-frequency component.

4.3 Modulation Indices

A good measure of the effects of the amplitude and phase modulations of the fundamental mode can be obtained from the amplitude and phase modulation indices. The amplitude modulation index, α is defined as

$$\alpha = \sqrt{E(a(t)^2 - a_0^2)}/a_0 \tag{4.1}$$

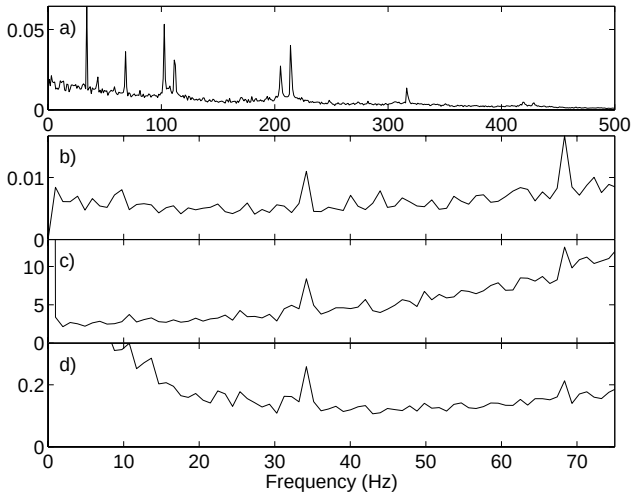

Figure 4.32: Unsteady Flow: Spectra at x=12.0 cm of a) the fluctuating component of velocity normalized by the velocity deficit b) the amplitude modulation c) the frequency modulation and d) the phase modulation

where the amplitude modulation of the fundamental is $a(t)$ and the mean of the amplitude modulation is a_0. The phase modulation index, β is defined as

$$\beta = \sqrt{E(p(t)^2 - p_0^2)} \tag{4.2}$$

where $p(t)$ is the phase modulation of the fundamental, and p_0 is the mean of the phase modulation.

Figure 4.33 shows the modulation indices as a function of location for the steady and unsteady cases. These are ensemble averages taken from twenty-four independent records of velocity fluctuations. Part a of the figure shows the modulation indices for the steady case and part b shows them for the unsteady case. The results show that, in the steady case, the index of the amplitude modulation decreases slightly in the linear region. Over the same region, $x < 5$ cm, the index of phase modulation increases. Between x = 5.0 cm and 8.0

cm, which corresponds to the second region of subharmonic growth both modulation indices have about the same value. Beyond 8.0 cm, the phase modulation index is larger indicating the redistribution of energy from the fundamental to its sidebands.

In the unsteady case, the modulation indices are significantly larger in the linear stage. This is in agreement with the analytical treatment of Hajj (1997). Beyond the linear region, the phase modulation index is significantly larger than the amplitude modulation index. In comparison with the steady case, the results show significantly larger phase modulation indices. This indicates that energy is redistributed from the fundamental to its sidebands faster in the unsteady case than in the steady case.

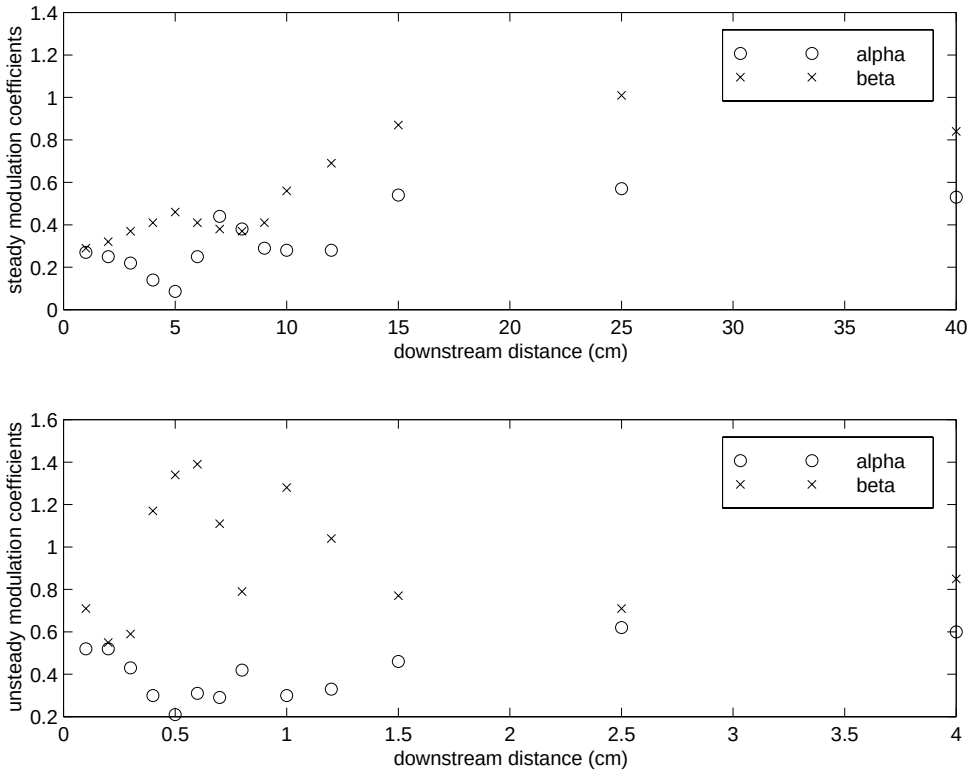

Figure 4.33: Modulation indicies as a function of downstream distance a) The steady case b) the unsteady case

Chapter 5

Time-varying Characteristics of Acoustically Forced Mixing Layers

In this chapter, wavelet analysis is performed on velocity fluctuations records from acoustically forced mixing layers. The acoustic forcing is applied at both the subharmonic and fundamental frequencies and more details on the experimental set-up are given in chapter 3. Two cases of phase excitations are considered. This allows us to determine the role of phase relation between the fundamental and the subharmonic on the transition characteristics and on the development of the subharmonic. These effects have been the subject of many studies, Patnaik, Sherman and Crocos(1976), Riley and Metcalf (1980), Arby and Ffowcs Williams (1984), Yang and Karlsson(1991) Rajaee and Karlsson(1992) and Hajj *et. al.* (1991,1993). Yet, to date, there has not been any characterization of the time-varying characteristics of the phase relation. In one of the two cases considered here, the phase of the fundamental is

set to $\frac{\pi}{2}$ and that of the subharmonic is set to zero at the excitation source. In the second case, the phase of the fundamental is set to $\frac{3\pi}{2}$ and that of the subharmonic is set to zero. We should stress here that these phases are expected to vary in the linear stability region. The reason being that the fundamental and the subharmonic travel at different phase speeds in these regions. Because the two modes have different frequencies, we will follow the work of Hajj *et. al.* (1993) and define the phase difference as the phase of the fundamental when the phase of the subharmonic is zero. Based on this definition and because the frequency of the fundamental mode is twice that of the subharmonic, the phase difference, ϕ, at any time is obtained by the difference, $\theta_f(t) - 2\theta_s(t)$, where $\theta_f(t)$ is the phase of the fundamental and $\theta_s(t)$ is the phase of the subharmonic. Also based on this definition, the case where the phase of the fundamental is set at $\frac{\pi}{2}$ and that of the subharmonic is set to zero will be referred to the case of $\frac{\pi}{2}$ phase difference at the excitation source. The other case will be referred to as the case of $\frac{3\pi}{2}$ phase difference at the excitation source.

The effects of acoustic forcing are analyzed at the same four locations considered in the previous chapter, x = 2.0, 5.0, 8.0 and 12.0 cm. As explained in chapter 4, these four locations correspond to stages of transition where different dynamics take place. The same wavelet parameters used in chapter 4 are also used here. In the discussion that follows, the role of phase relation in affecting the time variations or intermittency of the fundamental and subharmonic is examined. Measurements of the phase differences, ϕ, between the fundamental and the subharmonic are presented.

5.1 Case I: $\frac{\pi}{2}$ Phase Difference at the Excitation Source

The measured time series and the magnitude, real part and phase of the corresponding wavelet coefficients of velocity fluctuations are calculated for the case where the phase difference, ϕ, at the excitation source is set to $\frac{\pi}{2}$. The results from the downstream locations, x = 2.0, 5.0, 8.0 and 12 are shown in figures 5.1, 5.2, 5.3 and 5.4, respectively. In these figures, part a shows the normalized velocity fluctuations and parts b, c and d show the magnitude, real part and phase of the wavelet coefficients, respectively.

At x = 2.0 cm, the results in figure 5.1.b. show three distinct bands with relatively high levels of energy. These bands are at the scale given by ln(a) = 0.3, which corresponds to the fundamental mode, the scale given by ln(a) = 1, which corresponds to the subharmonic mode and the scale given by ln(a) = 1.6, which corresponds to the second subharmonic. The subharmonic has clearly the highest level of energy and is the least intermittent. On the other hand, the fundamental is quite intermittent, with large magnitudes near t = .02 s and t = .32 s and very small magnitudes near t = 0.2 s and t = 0.25 s. We note that the level of the second subharmonic is more easily discerned from the real part of the wavelet coefficients shown in figure 5.1.c than the magnitude shown in figure 5.1.b. This is due to the contrast between the positive and negative values. In figure 5.1.d, the phase shows a characteristic branching pattern. In general, the phase at a scale is determined by the largest frequency component at that scale. Thus, the branching represents a transition between scales where the second subharmonic is the largest frequency component and scales where the subharmonic dominates

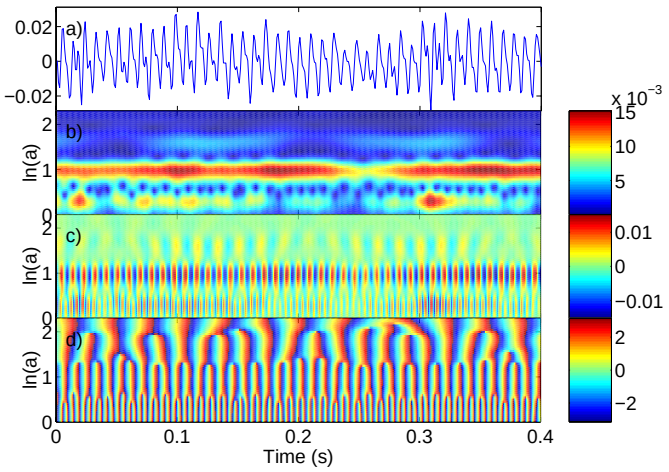

Figure 5.1: $\frac{\pi}{2}$ Forcing at x = 2.0 cm. a) The fluctuating component of velocity normalized by the velocity deficit b) the magnitude of the wavelet coefficients c) the real part of the wavelet coefficients and d) the phase of the wavelet coefficients

and even smaller scales where the fundamental dominates. The fact that lines of constant phase are nearly vertical in the scales that contain large fundamental and subharmonic components indicates that the magnitudes of the fundamental and subharmonic are much greater than their sidebands. The fact that lines of constant phase are not vertical at the scales above those that correspond to the subharmonic indicates that the energy contained in these scales is distributed over a range of frequency components.

By x = 5.0 cm, figure 5.2.b shows that the energy level of the fundamental is larger than that of the subharmonic. The energy level at the second subharmonic is relatively low. Neither the fundamental nor the subharmonic show significant intermittent characteristics. The variations seen in the scales larger than subharmonic in figures 5.2.c and 5.2.d occur at magnitudes that are too small to be considered significant.

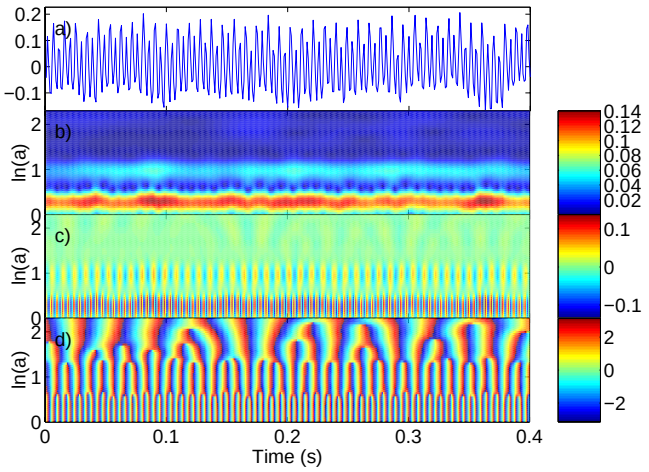

Figure 5.2: $\frac{\pi}{2}$ Forcing at x = 5.0 cm. a) The fluctuating component of velocity normalized by the velocity deficit b) the magnitude of the wavelet coefficients c) the real part of the wavelet coefficients and d) the phase of the wavelet coefficients

Results shown in figure 5.3 for the next location, x = 8.0 cm, indicate that the subharmonic has attained high levels of energy. Again, no intermittency is observed. Likewise, a consistent fundamental component is noted in the magnitude, real part and phase of the wavelet coefficients. In figure 5.3.d, the fundamental and the subharmonic mode seem to reach a phase value of zero at nearly the same time as can be seen from the colors.

By x = 12.0 cm, the results in figure 5.4.b show that the subharmonic is still the most energized component, but that it has become more intermittent. The fundamental is also quite intermittent. In figure 5.4.c, low frequency components are apparent, particularly at the second subharmonic. The phase synchronization observed at x = 8.0 cm can also be noted in figure 5.4.d as well. There is also evidence in figure 5.4.d that components with frequencies higher than that of the fundamental frequency have a relatively high level of

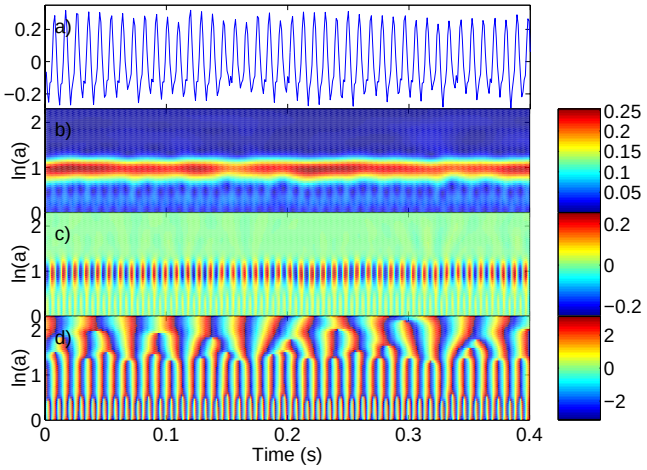

Figure 5.3: $\frac{\pi}{2}$ Forcing at x = 8.0 cm. a) The fluctuating component of velocity normalized by the velocity deficit b) the magnitude of the wavelet coefficients c) the real part of the wavelet coefficients and d) the phase of the wavelet coefficients

energy. The main evidence for this is the branching in the phase at the scales near ln(a) = 0.1.

The time variations of the magnitude, real part and phase at the scales corresponding to the fundamental and the subharmonic modes are shown in the next series of plots. Figures 5.5 and 5.6 show respectively the variations of the fundamental and subharmonic modes at x = 2.0 cm. The same variations at x = 5.0, 8.0 and 12.0 cm are shown in figures 5.7 and 5.8, 5.9 and 5.10, and 5.11 and 5.12, respectively. In these figures, the velocity fluctuations are shown in part a, the magnitude is shown in part b, the real part is shown in part c, and the phase lag is shown in part d. The phase lag is the phase of the wavelet coefficients with the carrier frequency of that scale removed.

At x = 2.0 cm, a comparison of the plots of the real parts of the fundamental and the

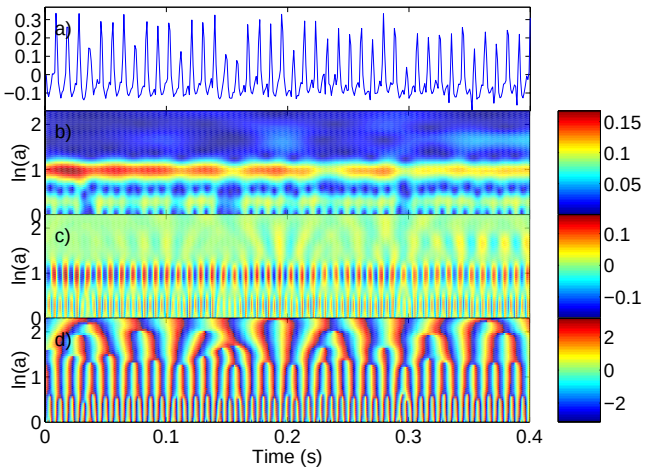

Figure 5.4: $\frac{\pi}{2}$ Forcing at x = 12.0 cm. a) The fluctuating component of velocity normalized by the velocity deficit b) the magnitude of the wavelet coefficients c) the real part of the wavelet coefficients and d) the phase of the wavelet coefficients

subharmonic, figures 5.5.c and 5.6.c, respectively, shows that the subharmonic is both larger and less intermittent than the fundamental. The time variations shown in figures 5.5.d and 5.6.d show that, at this location, the phases of the fundamental and the subharmonic do not show significant variations. By x = 5.0 cm, a comparison of figures 5.7b and 5.8b shows that the magnitude of the fundamental is larger than the magnitude of the subharmonic. This is expected since the fundamental mode is the most unstable. As for the phase variations with time at this location, figures 5.7.d and 5.8.d show that there is basically no variation with time.

At x = 8.0 cm, figures 5.9.b and 5.10.b show that the magnitude of the subharmonic is significantly larger than that of the fundamental. This results in a variation of the magnitude and phase of the fundamental, shown in figures 5.9.b and 5.9.d. Based on equation 2.20,

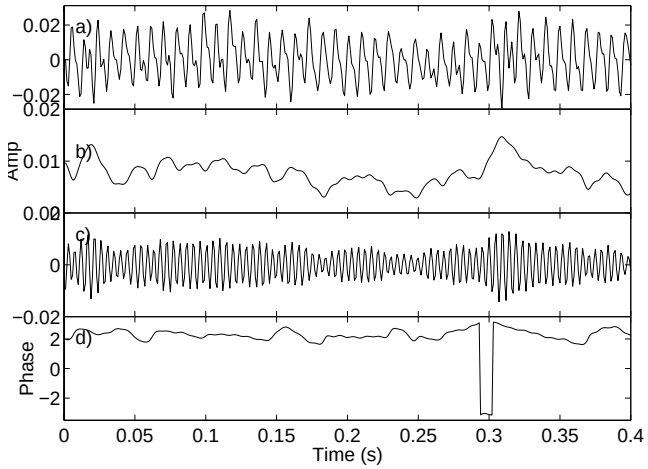

Figure 5.5: $\frac{\pi}{2}$ Forcing: Time-variations of the fundamental at x = 2.0 cm. a) The fluctuating component of velocity normalized by the velocity deficit b) the magnitude of wavelet coefficients c) the real part of wavelet coefficients and d) the phase lag from wavelet coefficients

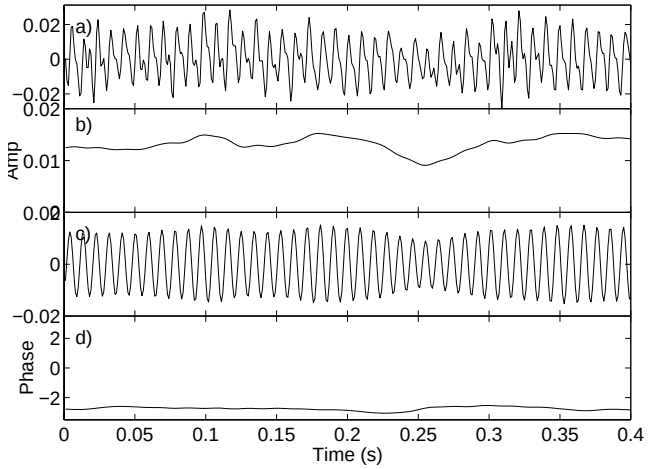

Figure 5.6: $\frac{\pi}{2}$ Forcing: Time-variations of the subharmonic at x = 2.0 cm. a) The fluctuating component of velocity normalized by the velocity deficit b) the magnitude of wavelet coefficients c) the real part of wavelet coefficients and d) the phase lag from wavelet coefficients

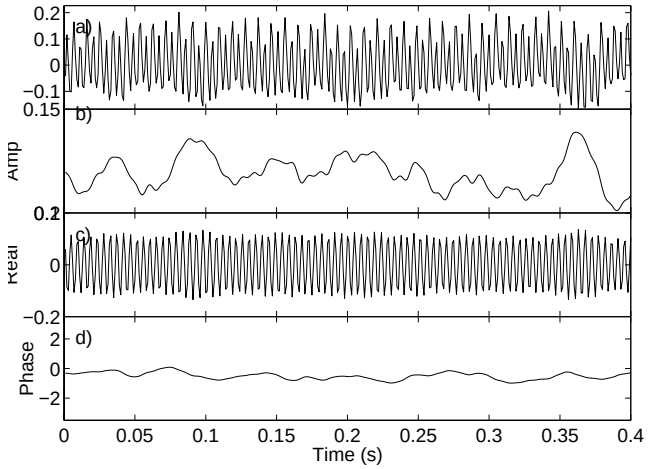

Figure 5.7: $\frac{\pi}{2}$ Forcing: Time-variations of the fundamental at x = 5.0 cm. a) The fluctuating component of velocity normalized by the velocity deficit b) the magnitude of wavelet coefficients c) the real part of wavelet coefficients and d) the phase lag from wavelet coefficients

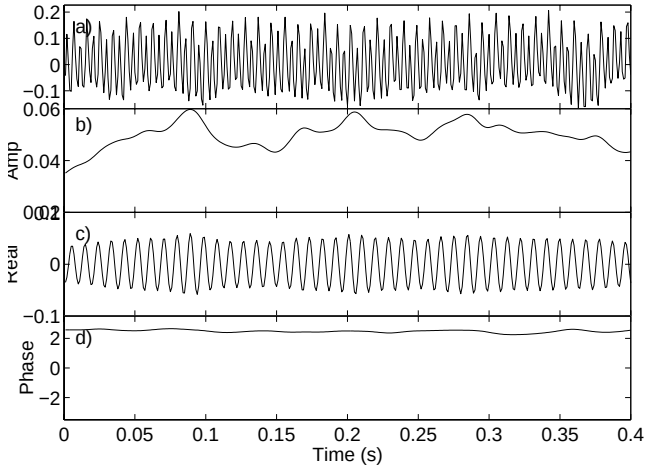

Figure 5.8: $\frac{\pi}{2}$ Forcing: Time-variations of the subharmonic at x = 5.0 cm. a) The fluctuating component of velocity normalized by the velocity deficit b) the magnitude of wavelet coefficients c) the real part of wavelet coefficients and d) the phase lag from wavelet coefficients

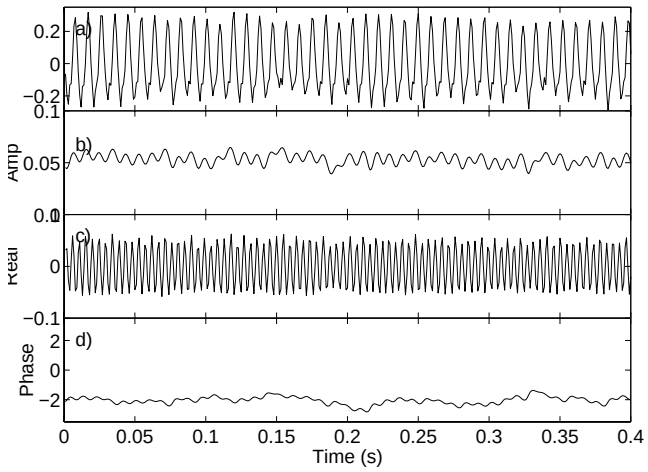

Figure 5.9: $\frac{\pi}{2}$ Forcing: Time-variations of the fundamental at x = 8.0 cm. a) The fluctuating component of velocity normalized by the velocity deficit b) the magnitude of wavelet coefficients c) the real part of wavelet coefficients and d) the phase lag from wavelet coefficients

at the scale with a peak frequency equal to the fundamental frequency, the magnitude of the subharmonic frequency is attenuated 97.6% and the fundamental is unattenuated. Yet, because the magnitude of the unattenuatted subharmonic, shown in figure 5.10.b, is about $.25\Delta U$, the subharmonic contribution to this scale is on the order of $.006\Delta U$. This is large enough to be noticeable, since the magnitude of the fundamental is only about $.05\Delta U$. Thus, the variations of the fundamental at this location can to some extent be related to the subharmonic component.

At x = 12.0 cm, the results in figures 5.11.b and 5.12.b, show that the magnitudes of both the fundamental and the subharmonic have significant low frequency variations. These larger variations in amplitude, however, correspond to only small variations in phase as can be seen in figures 5.11.d and 5.12.d.

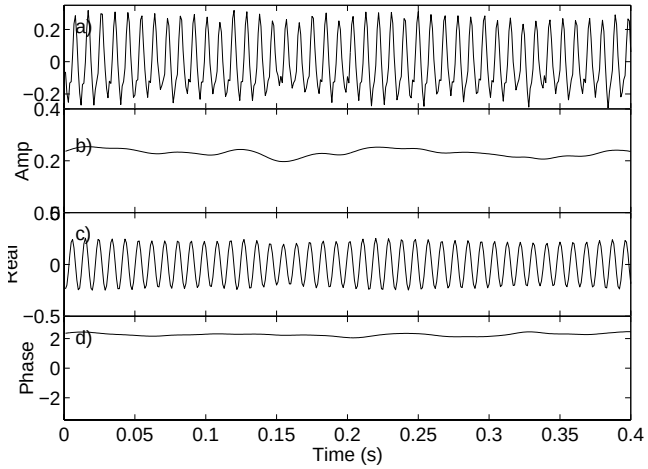

Figure 5.10: $\frac{\pi}{2}$ Forcing: Time-variations of the subharmonic at x = 8.0 cm. a) The fluctuating component of velocity normalized by the velocity deficit b) the magnitude of wavelet coefficients c) the real part of wavelet coefficients and d) the phase lag from wavelet coefficients

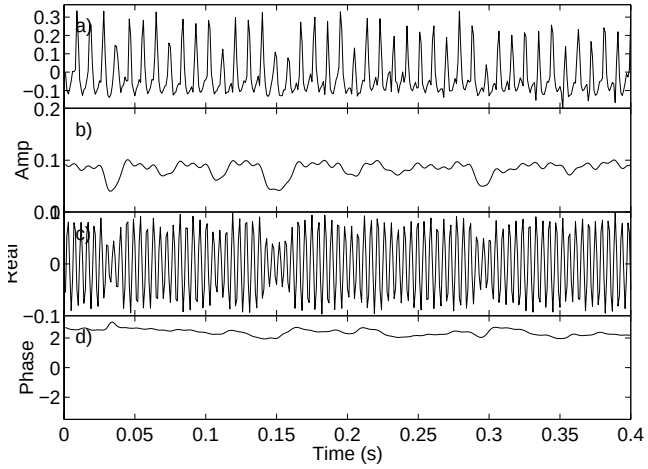

Figure 5.11: $\frac{\pi}{2}$ Forcing: Time-variations of the fundamental at x = 12.0 cm. a) The fluctuating component of velocity normalized by the velocity deficit b) the magnitude of wavelet coefficients c) the real part of wavelet coefficients and d) the phase lag from wavelet coefficients

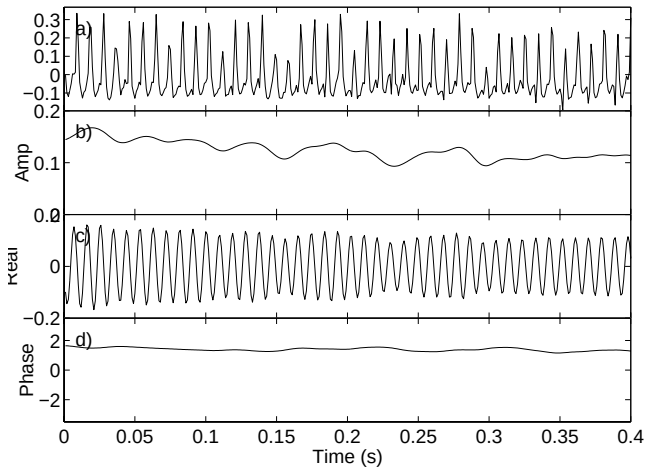

Figure 5.12: $\frac{\pi}{2}$ Forcing: Time-variations of the subharmonic at x = 12.0 cm. a) The fluctuating component of velocity normalized by the velocity deficit b) the magnitude of wavelet coefficients c) the real part of wavelet coefficients and d) the phase lag from wavelet coefficients

The time variations of the phase difference, ϕ, defined as $\theta_f - 2\theta_s$ at several downstream locations are shown in figure 5.13. The results clearly show that in the linear stability region, $x \leq 4.0$ cm, the phase relation varies from ϕ being about π radians at x = 1.0 cm to a value of 1 radian at x = 4.0 cm. Between x = 4.0 cm and 12.0 cm, the phase values remain near zero at all locations. The results also show small intermittent variations at x = 1.0 cm. Between x = 2.0 cm and 12.0 cm, the results show no time varying characteristics for the phase difference, ϕ. At x = 15.0 cm, intermittent variations are noted. The fact that the phase varies little in time or with downstream distance indicates a high level of coupling between the fundamental and the subharmonic components that results in the enhanced growth of the subharmonic.

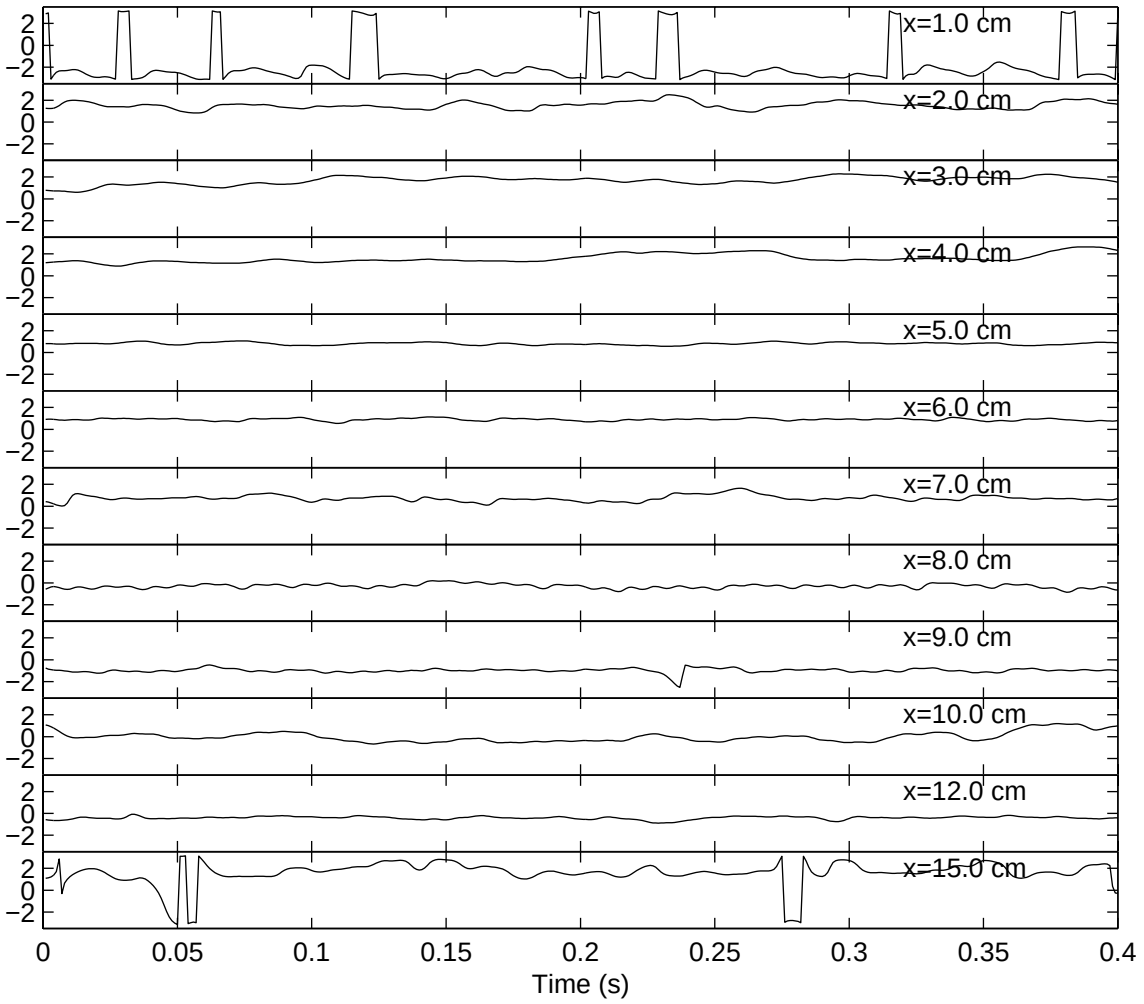

Figure 5.13: $\frac{\pi}{2}$ Forcing: Phase Relation, ϕ, of the fundamental and the subharmonic at several downstream locations.

5.2 Case II: $\frac{3\pi}{2}$ Phase Difference at Excitation Source

The measured time series and the magnitude, real part and phase of the corresponding wavelet coefficients of velocity fluctuations are examined for the case where the phase relation at the excitation source is set to $\frac{3\pi}{2}$. Results for the downstream locations, x = 2.0, 5.0, 8.0 and 12 are shown in figures 5.14, 5.15, 5.16 and 5.17, respectively. Part a shows the normalized velocity fluctuations, and parts b, c and d show the magnitude, real part and phase of the wavelet coefficients respectively.

At x = 2.0 cm, the same three bands that were noted in the $\frac{\pi}{2}$ case are also observed in this case, figure 5.14.b. It is not surprising that the plots are qualitatively similar at this location, because the fundamental and subharmonic are growing independently. Thus, their phase relation should not significantly alter the magnitude of the velocity fluctuations. A comparison of figures 5.1.d and 5.14.d shows that the phase relation of fundamental and subharmonic is near zero in the $\frac{3\pi}{2}$ case and near 1 radian in the $\frac{\pi}{2}$ case.

At x = 5.0 cm, the magnitude of the wavelet coefficients in the $\frac{3\pi}{2}$ forcing case, shown in figure 5.15.b, still bears a strong resemblance to its $\frac{\pi}{2}$ forcing counterpart, shown in figure 5.2.b. Both the subharmonic and the fundamental modes have somewhat less energy than in the $\frac{3\pi}{2}$ case. The phase relation between the fundamental and subharmonic is similar to the one observed at x = 2.0 cm as can be seen from parts d of figures 5.15 and 5.14.

By x = 8.0 cm, there is a difference between the magnitude of subharmonic mode in the $\frac{3\pi}{2}$ forcing case, shown in figure 5.16.b and that observed in the $\frac{\pi}{2}$ forcing case shown in figure

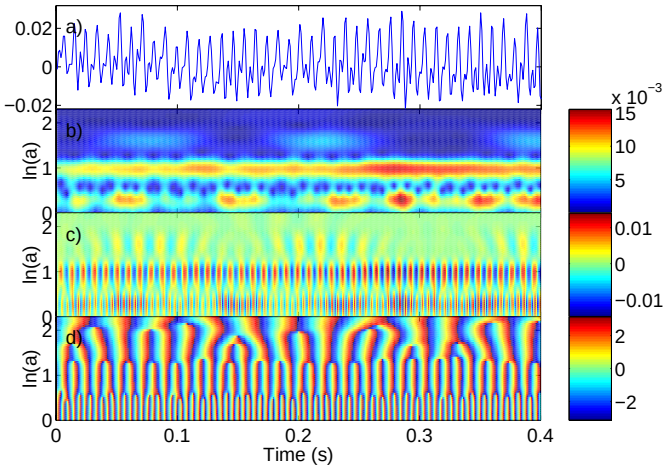

Figure 5.14: $\frac{3\pi}{2}$ Forcing at x = 2.0 cm. a) The fluctuating component of velocity normalized by the velocity deficit b) the magnitude of the wavelet coefficients c) the real part of the wavelet coefficients and d) the phase of the wavelet coefficients

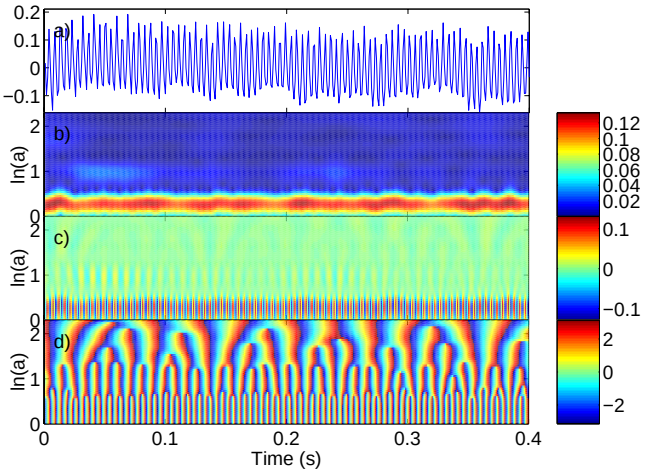

Figure 5.15: $\frac{3\pi}{2}$ Forcing at x = 5.0 cm. a) The fluctuating component of velocity normalized by the velocity deficit b) the magnitude of the wavelet coefficients c) the real part of the wavelet coefficients and d) the phase of the wavelet coefficients

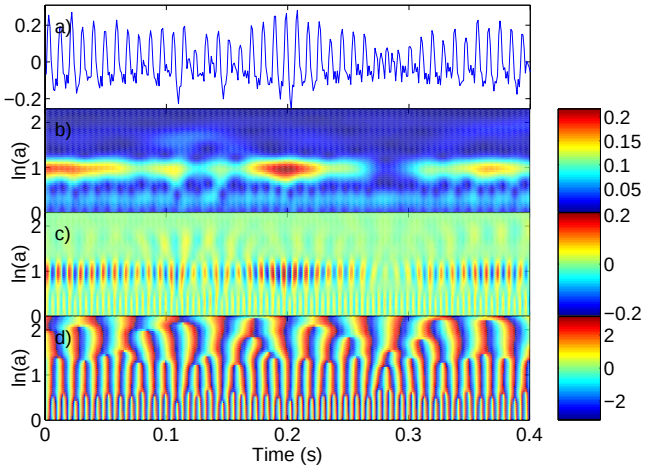

Figure 5.16: $\frac{3\pi}{2}$ Forcing at x = 8.0 cm. a) The fluctuating component of velocity normalized by the velocity deficit b) the magnitude of the wavelet coefficients c) the real part of the wavelet coefficients and d) the phase of the wavelet coefficients

5.3.b. The subharmonic in the $\frac{3\pi}{2}$ forcing case is significantly more intermittent than the $\frac{\pi}{2}$ forcing case. Also, the phase relation between the subharmonic and the fundamental in the $\frac{\pi}{2}$ case, shown in figure 5.3.d has shifted so that the phases of the subharmonic and the fundamental are near zero at the same times.

At x = 12.0 cm, the magnitudes, shown in figure 5.17.b, of the subharmonic and the fundamental are much more intermittent than those in the $\frac{\pi}{2}$ forcing case. A comparison of the phases of the fundamental and the subharmonic for the $\frac{\pi}{2}$ and $\frac{3\pi}{2}$ forcing cases, shows that many more frequency components are present in the $\frac{3\pi}{2}$ case, as indicated by the more varied branching pattern in the phase of the wavelet coefficients.

Time variations of the magnitude, real part and phase of the wavelet coefficients at the scales corresponding to the fundamental and the subharmonic modes are shown in the next

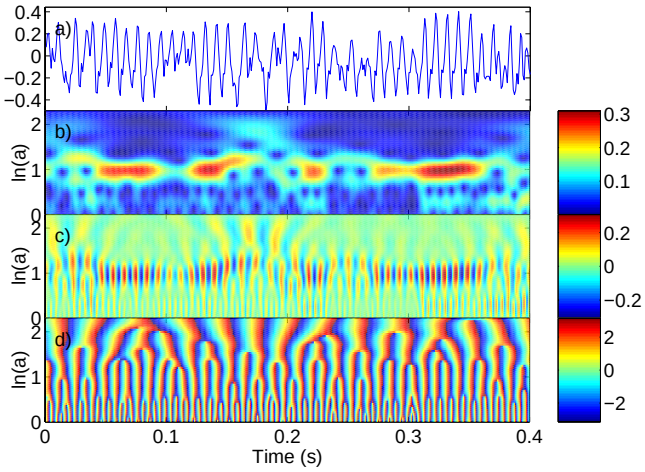

Figure 5.17: $\frac{3\pi}{2}$ Forcing at x = 12.0 cm. a) The fluctuating component of velocity normalized by the velocity deficit b) the magnitude of the wavelet coefficients c) the real part of the wavelet coefficients and d) the phase of the wavelet coefficients

series of figures. The variations at x = 2.0 cm are shown in figure 5.18 for the fundamental and figure 5.19 for the subharmonic. The same variations at x = 5.0, 8.0 and 12.0 cm are shown in figures 5.20 and 5.21, 5.22 and 5.23, and 5.24 and 5.25, respectively. In these plots, the velocity fluctuations are shown in part a, the magnitude is shown in part b, the real part in part c, and the phase of the wavelet coefficients with either the fundamental or the subharmonic removed in part d.

At x = 2.0 cm, a comparison of the plots of the magnitudes of the fundamental and the subharmonic, figures 5.18.b and 5.19.b, shows that as in the $\frac{\pi}{2}$ forcing case, the subharmonic is larger and less intermittent. A comparison of the phases of the fundamental and the subharmonic in the $\frac{3\pi}{2}$ forcing case with their counter parts in the $\frac{\pi}{2}$ forcing case shows that while the phases differ, the level of variability is about the same.

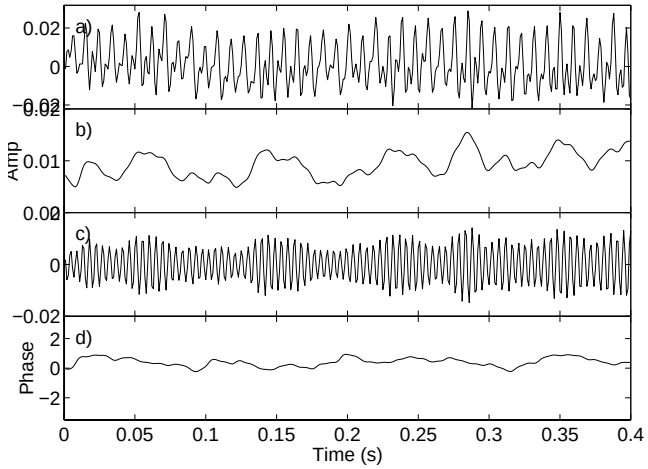

Figure 5.18: $\frac{3\pi}{2}$ Forcing: Time-variations of the fundamental at x = 2.0 cm. a) The fluctuating component of velocity normalized by the velocity deficit b) the magnitude of wavelet coefficients c) the real part of wavelet coefficients and d) the phase lag from wavelet coefficients

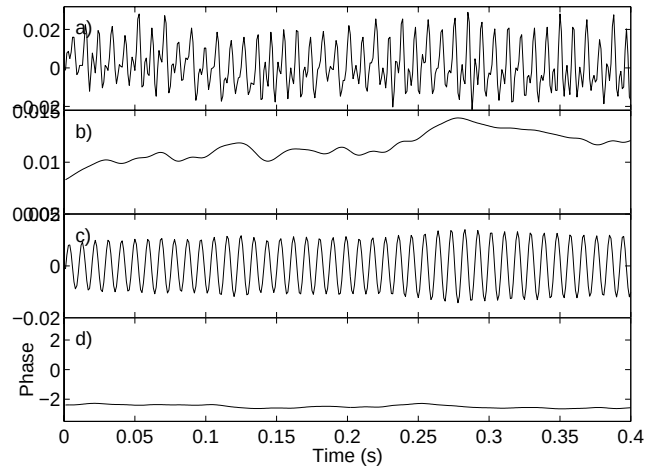

Figure 5.19: $\frac{3\pi}{2}$ Forcing: Time-variations of the subharmonic at x = 2.0 cm. a) The fluctuating component of velocity normalized by the velocity deficit b) the magnitude of wavelet coefficients c) the real part of wavelet coefficients and d) the phase lag from wavelet coefficients

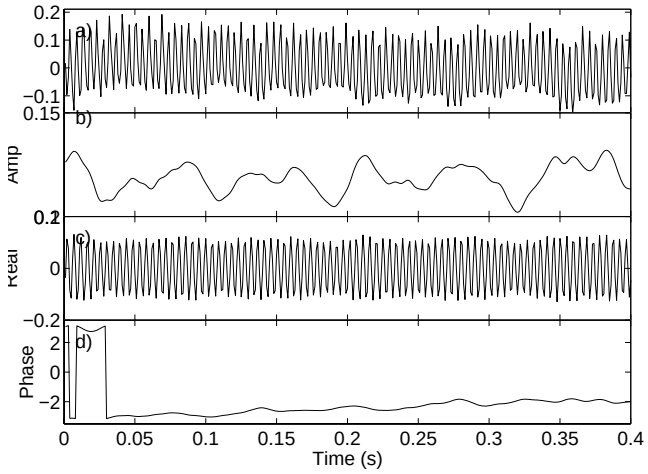

Figure 5.20: $\frac{3\pi}{2}$ Forcing: Time-variations of the fundamental at x = 5.0 cm. a) The fluctuating component of velocity normalized by the velocity deficit b) the magnitude of wavelet coefficients c) the real part of wavelet coefficients and d) the phase lag from wavelet coefficients

At x = 5.0 cm, the magnitude of the fundamental, shown in figure 5.20.b is significantly larger than that of the subharmonic, shown in figure 5.21.b. The magnitude of the subharmonic in the $\frac{3\pi}{2}$ case shows more variations in time than in the $\frac{\pi}{2}$ case. The jumps in the phase of the fundamental observed in the first part of the record shown in figure 5.20.d are between π and $-\pi$ and are therefore not physical discontinuities. We should note the slight trend in the phase of the fundamental and the large jump near t = 0.35 s in the phase of the subharmonic.

By x = 8.0 cm, the magnitude of the subharmonic, shown in figure 5.22.b, is considerably larger than the fundamental, shown in figure 5.23.b. As in the $\frac{\pi}{2}$ forcing case, this large value of the magnitude of the subharmonic seems to introduce variations in the magnitude of the fundamental. Even without these variations, the magnitude and phase of the fundamental

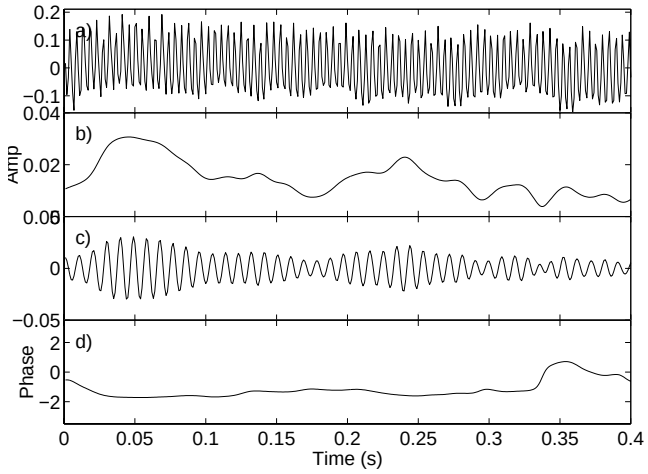

Figure 5.21: $\frac{3\pi}{2}$ Forcing: Time-variations of the subharmonic at x = 5.0 cm. a) The fluctuating component of velocity normalized by the velocity deficit b) the magnitude of wavelet coefficients c) the real part of wavelet coefficients and d) the phase lag from wavelet coefficients

has a higher level of variability in the $\frac{3\pi}{2}$ case than in the $\frac{\pi}{2}$ case. Also, the magnitude of the $\frac{3\pi}{2}$ subharmonic appears more variable than its $\frac{\pi}{2}$ counter part.

At x = 12.0 cm, the magnitudes of the fundamental, shown in figure 5.24.b, and the subharmonic, shown in figure 5.25.b, are considerably more variable than their $\frac{\pi}{2}$ forcing case counterparts, shown in figures 5.11.b and 5.12.b, respectively. We note the presence of overmodulations in the fundamental near t = .26 s and in the subharmonic near t = 0.03, 0.04, 0.17, 0.20, 0.24, 0.26 and 0.37 s. The presence of such a large number of overmodulations is an indication that subharmonic sidebands have significant energy. The magnitude of the subharmonic in the $\frac{3\pi}{2}$ case is much more intermittent than its counterpart in the $\frac{\pi}{2}$ case.

The time variations of the phase relation, ϕ, between the fundamental and the subharmonic

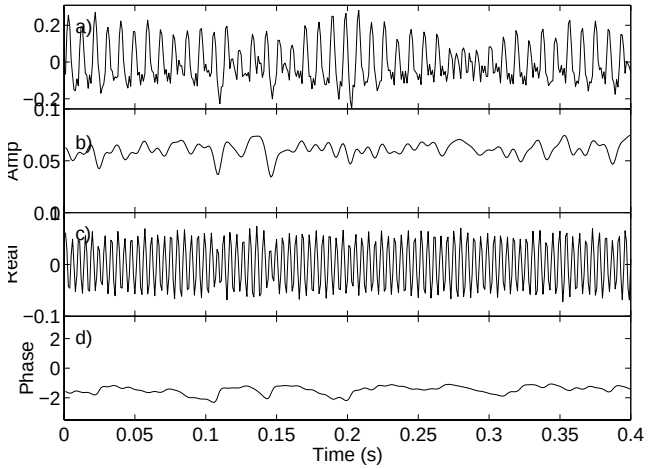

Figure 5.22: $\frac{3\pi}{2}$ Forcing: Time-variations of the fundamental at x = 8.0 cm. a) The fluctuating component of velocity normalized by the velocity deficit b) the magnitude of wavelet coefficients c) the real part of wavelet coefficients and d) the phase lag from wavelet coefficients

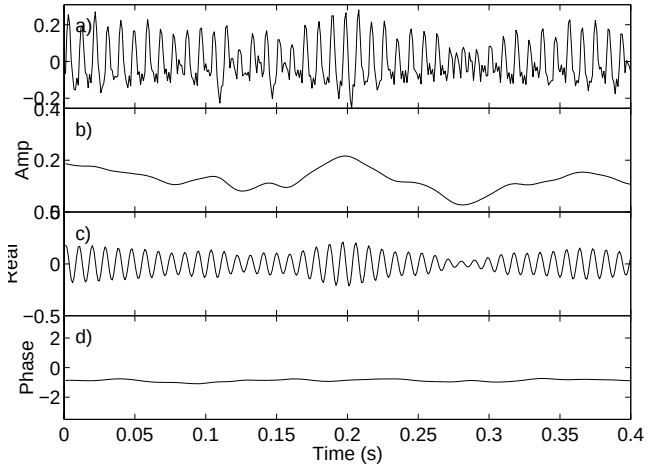

Figure 5.23: $\frac{3\pi}{2}$ Forcing: Time-variations of the subharmonic at x = 8.0 cm. a) The fluctuating component of velocity normalized by the velocity deficit b) the magnitude of wavelet coefficients c) the real part of wavelet coefficients and d) the phase lag from wavelet coefficients

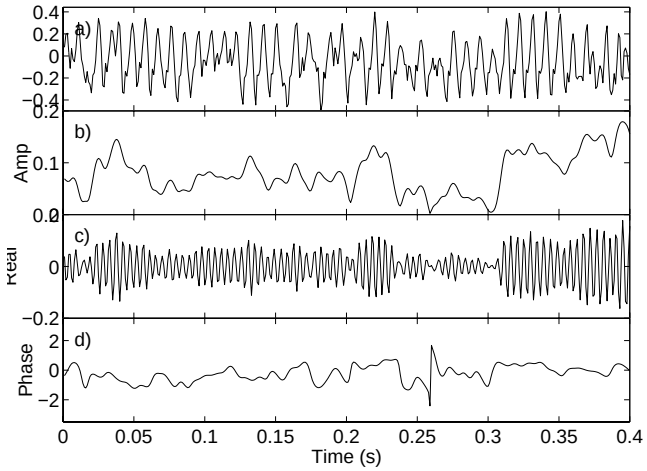

Figure 5.24: $\frac{3\pi}{2}$ Forcing: Time-variations of the fundamental at x = 12.0 cm. a) The fluctuating component of velocity normalized by the velocity deficit b) the magnitude of wavelet coefficients c) the real part of wavelet coefficients and d) the phase lag from wavelet coefficients

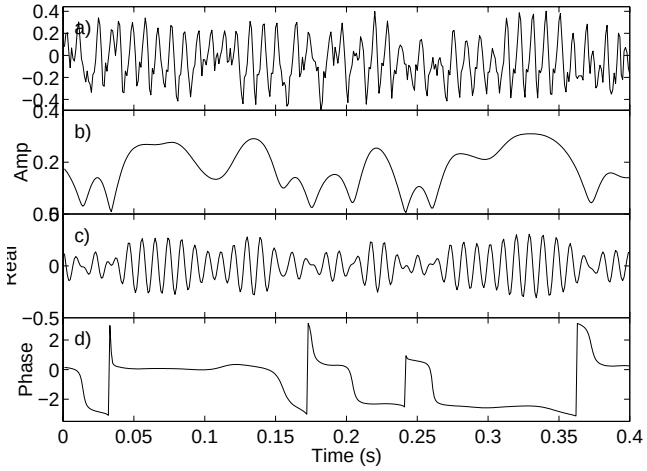

Figure 5.25: $\frac{3\pi}{2}$ Forcing: Time-variations of the subharmonic at x = 12.0 cm. a) The fluctuating component of velocity normalized by the velocity deficit b) the magnitude of wavelet coefficients c) the real part of wavelet coefficients and d) the phase lag from wavelet coefficients

at different downstream locations is shown in figure 5.26. As in the case of the $\frac{\pi}{2}$ forcing, the phase difference shows variations between x = 1.0 and 4.0 cm. Moreover, the phase difference undergoes more variations with time in the $\frac{3\pi}{2}$ forcing case than in the $\frac{\pi}{2}$ forcing case. This is most clearly observed at x = 4.0 cm. According to Hajj *et. al* (1992,1993), this location is near the end of the linear stability region. Thus, it would have a significant effect on the subsequent development of the subharmonic. Hajj *et al.* (1993) showed that, in the $\frac{3\pi}{2}$ forcing case, the subharmonic undergoes equilibration at this location while in the $\frac{\pi}{2}$ case, it undergoes continuous growth. Thus the observed time variations in ϕ indicate that they affect the subharmonic growth and the larger they are, the more the subharmonic growth is delayed.

5.3 Statistical Summary

A more quantitative description of the variations in the phase relation is obtained from mean and standard deviations of the phase relation from eight records. A summary of the statistical description of the phase difference in the $\frac{\pi}{2}$ and the $\frac{3\pi}{2}$ cases is shown in figure 5.27. Part a shows the mean obtained over eight records as a function of downstream distance, x. Part b shows the standard deviation obtained over the same records.

The mean phase relation, ϕ, shown in figure 5.27.a appears to vary significantly between x = 1.0 cm to x = 3.0 cm in both cases. After this location, the $\frac{\pi}{2}$ case maintains a nearly constant phase of about .9 radians, and the $\frac{3\pi}{2}$ increases until it reaches approximately the

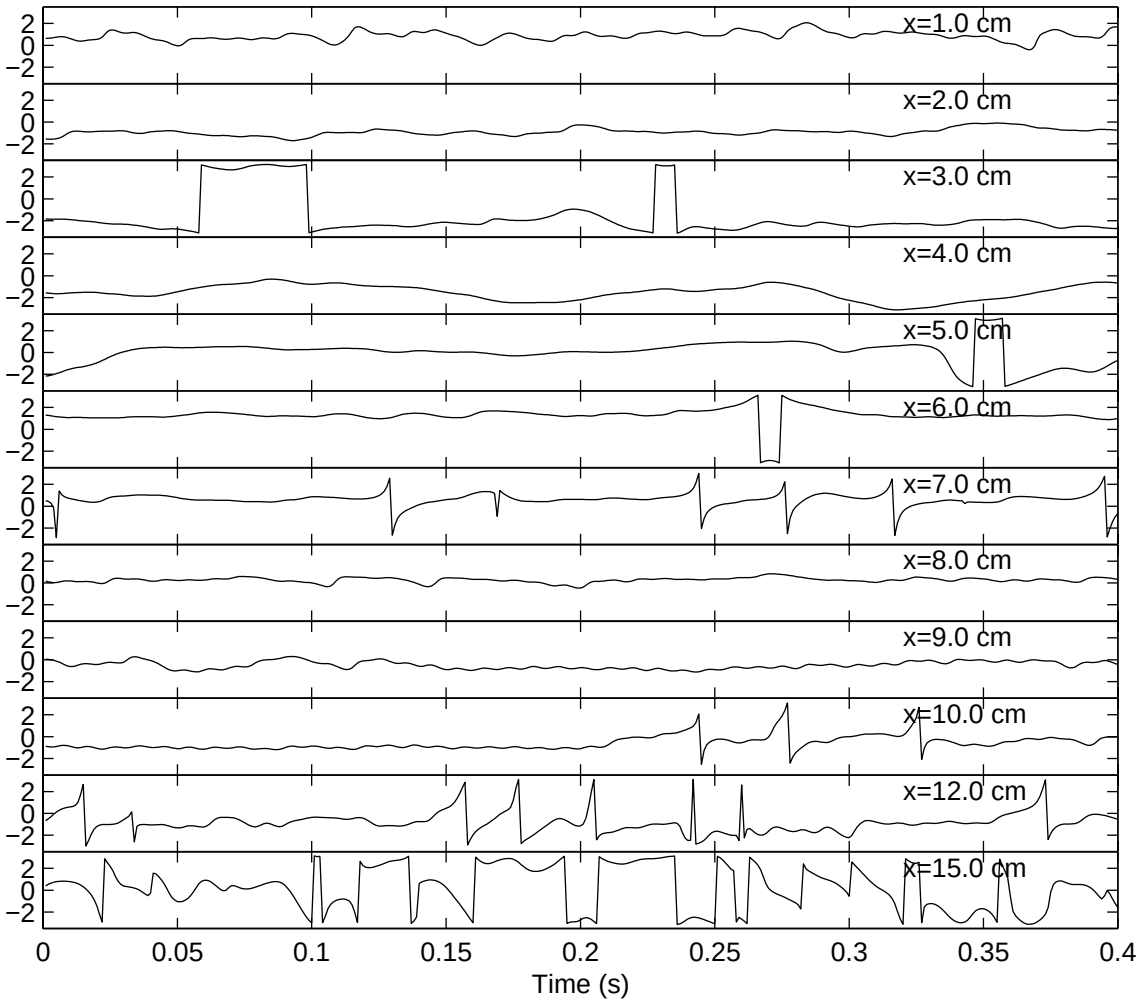

Figure 5.26: $\frac{3\pi}{2}$ Forcing: Phase Relation, ϕ, of the fundamental and the subharmonic at different downstream locations

same phase, .9 radians near x = 6 cm. The results for downstream locations beyond x = 6 cm are similar for both cases. Figure 5.27.b shows the standard deviations of the variations over the eight records taken at each location. The decreasing variability with time of the $\frac{\pi}{2}$ case as a function of distance in the initial regions of the flow indicates that the time variations of the phase relation decrease as the phase approaches .9 radians. On the other hand, the time variability of the $\frac{3\pi}{2}$ case increases as the phase approaches the .9 radian value, and decreases sharply when the .9 radian value is attained.

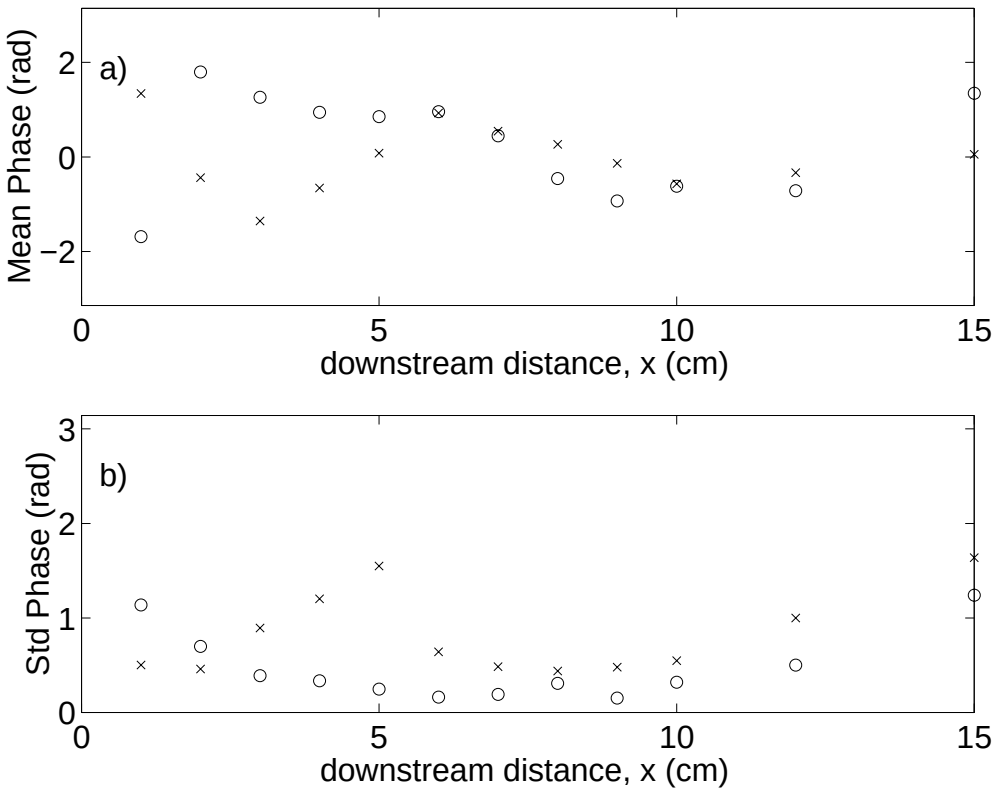

Figure 5.27: Statistical description of the phase relation, $\phi(t)$, in the $\frac{\pi}{2}$ case, represented with an o, and the $\frac{3\pi}{2}$ case, represented with an x, a) The mean of $\phi(t)$ and b) standard deviation of $\phi(t)$, as a function of downstream distance x.

Chapter 6

Wavelet Based Decomposition of Propagating Waves

In this chapter, we show how temporal information obtained by wavelet analysis can be used to separate propagating waves. The analysis presented here does not have any limitations on the direction of the two waves or their frequencies. The only limitation is that the two waves reach the point of measurement at different times. The two waves considered here are propagating in opposite directions simply because it is a more challenging problem. In particular, we show how information from the phase of the wavelet is used to separate the two components.

The signal generated by two waves propagating in opposite directions is given by

$$\eta_C(x,t) = \eta_1(x,t)+\eta_2(x,t) = \alpha_1 cos(2\pi f_g t+k_0 x+\phi_1)+H(t-t_0)\alpha_2 cos(2\pi f_g t-k_0 x+\phi_2) \quad (6.1)$$

where α_1 and α_2 denote the amplitude of the first and second waves and ϕ_1 and ϕ_2 denote their corresponding phases, $H(t-t_0)$ is a step function, which is equal to zero for $t \leq t_0$ and is equal to one for $t > t_0$. The wave number, k_0 and frequency, f_g are the same for the two waves. If k_0 was different for each wave, Fourier domain analysis of measurements from two points would be adequate to decompose the waves. But, since they have the same frequency and wavenumber, Fourier analysis cannot be used.

When measurements are taken at a single location, x_0, kx_0 is a constant and can be absorbed into the phase. Equation 6.1 can then be written for any location as a function of time only, i.e.

$$\eta_C(t) = \alpha_C cos(2\pi f_g t + \phi_C) = \alpha_1 cos(2\pi f_g t + \phi_1) + H(t-t_0)\alpha_2 cos(2\pi f_g t + \phi_2). \qquad (6.2)$$

A measuring device located at x_0, would record instantaneous values of η_C. Since for $t < t_0$, $\eta_C(t) = \eta_1(t)$, the only unknown left to be determined is $\eta_2(t)$. One can find t_0, α_C, α_1, ϕ_C and ϕ_1 from wavelet analysis of $\eta_C(t)$. To illustrate how the amplitudes and phases of the two waves interact to produce the combined wave, equation 6.2 is represented pictorially in figure 6.1. From that figure, it is obvious that when α_C, α_1, ϕ_C and ϕ_1 are known, α_2, ϕ_2 can be obtained.

To illustrate the above argument, we perform wavelet analysis on a numerical example. In this example, the nondimensional amplitude of the first wave, α_1, is 10 and its phase, ϕ_1, is zero. The nondimensional amplitude of the second wave, α_2 is 5 and its phase, ϕ_2 is 1.8235 radians. The nondimensional frequency of both components, f_g is set at .5. The

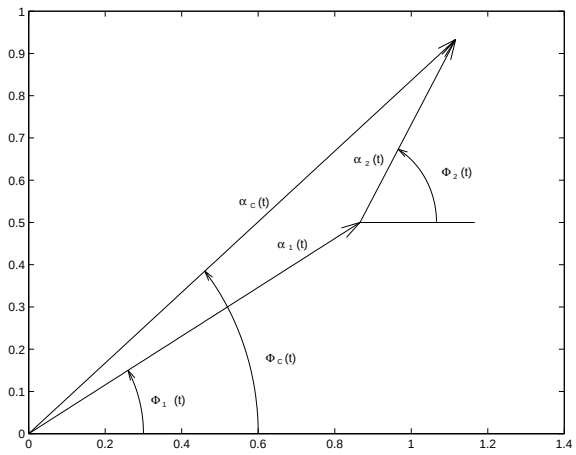

Figure 6.1: Vectorial representation of $\eta_C(x,t)$

nondimensional time for the start of the second wave is set to be $t = 30$.Figure 6.2 shows the first wave in part a, the second wave in part b and the combination of the two waves in part c. Because of the choice of the phase, ϕ_2, the second component does not affect the amplitude. This is not a limitation of the technique and a change in amplitude would probably be encountered in a real situation. We have opted for this choice to show the effectiveness of the analysis in an extreme situation.

The original signal, $\eta_C(t)$, is plotted in figure 6.3 a. In figure 6.3 b, the magnitude of the wavelet coefficients is plotted. Note that the scale has been normalized to yield magnitudes equal to the amplitude of η_C. The first amplitude is measured as 10, and the corresponding phase is zero, which are the input values for the first component. The time when the second component was introduced can be determined as $t_0 = 30$ from the location of the phase shift in figure 6.3 c. As explained in section 2.2.4, discontinuities are smoothed over the

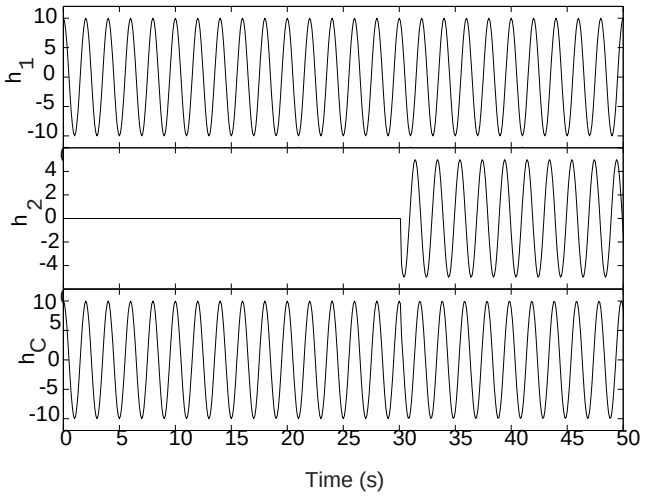

Figure 6.2: Wave superposition: Part a) $\eta_1(t) = 10cos(2\pi.5t)$ b) $\eta_2(t) = 5cos(2\pi.5t + 1.82)$ Part c) η_C

temporal support of the wavelet. The combined amplitude is also 10 but the combined phase is measured as .5054 radians. Based on the vectorial representation shown in figure 6.1, the amplitude and phase of the second wave can be recovered as 5.0 and 1.8235 radians, respectively.

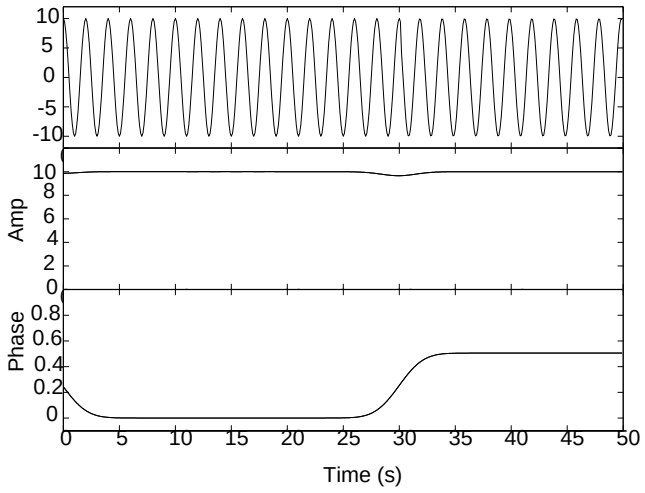

Figure 6.3: Wave superposition recovery: Part a) $\eta_C(t)$ Part b) The amplitude modulation from wavelets Part c) the phase modulation from wavelets

Chapter 7

Conclusions

In this work, wavelet analysis is used to determine time-varying characteristics in terms of amplitude, phase and frequency modulations. The analysis is implemented in transistioning mixing layers under different mean flow and component excitation conditions. The analysis and in particular, instantaneous phase change are used to separate propagating waves. In summary, the results presented here show that

- the wavelet coefficients can be calculated more efficiently in the Fourier domain than in the time domain. Wavelet parameters needed for these calculations are presented and verified. Analytic signals are examined to determine the error levels in using the wavelets (or scale representation) to determine modulation characteristics of frequency components.

- From the analysis of the velocity fluctuations of transistioning steady mixing layers,

it is concluded that beyond the initial region of linear stability, the growth of the fundamental and subharmonic modes is synchronized in time. This synchronization is evidence of the parametric interaction between these modes. In this mechanism, an enhanced fundamental component leads to the growth of the subharmonic component.

- From the analysis of the velocity fluctuations of transistioning unsteady mixing layers, it is shown that the mean flow unsteadiness results in enhanced amplitude and phase modulations of the fundamental mode througout the transistion. These results are in agreement with the analysis presented by Hajj(1997).

- From the analysis of the velocity fluctuations of the acoustically forced mixing layers, it is shown that selective forcing can produce time-variations in the phase relations between the fundamental and the subharmonic modes. These variations lead to enhanced or suppressed growth rates of the subharmonic in the secondary instability region.

- Finally, we used the magnitude and phase of the wavelet coefficients to decompose two waves with the same frequency and wavenumber that propagate in opposite directions and reach the point of measurement at different times.

References

Arby, H. and Ffowcs Williams, J. D. 1984 Active cancellation of pure tones in an excited jet. *J. Fluid Mech.* **149**, 445-454.

Gabor, D. 1946 Theory of Communication. *J. of IEEE*, **93**, 429-457.

Hajj, M.R., Miksad, R.W. and Powers, E.J. 1991 Experimental investigation of the fundamental-subharmonic coupling: effect of the initial phase difference. *AIAA Paper* 91-0624.

Hajj, M.R., Miksad, R.W. and Powers, E.J. 1992 Subharmonic growth by parametric resonance *J. Fluid Mech.* **236**, 385.

Hajj, M.R., Miksad, R.W. and Powers, E.J. 1992 Fundamental-subharmonic interaction: effect of phase relation *J. Fluid Mech.* **256**, 403.

Hajj, M.R. 1997 Stability characteristics of a periodically unsteady mixing layer" *Phys. Fluids* **9** (2).

Jones, F.L., 1983, Experimental Study of Nonlinear Wave Interactions and Modulations During Transition of a Symmetric Wake Ph.D. dissertation, the University of Texas at Austin.

Jordan, D., Miksad, R.W. and Powers, E.J. 1997 Implementation of the Continuous Wavelet Transform for Digital Time Series Analysis *Rev. Sci. Instrum.* **68**, 1484-1494.

Kim, Y.C., Khadra, L. and Powers, E.J. 1980 Wave modulation in a nonlinear dispersive medium. *Phys. Fluids* **23**, 2250-2257.

Miksad, R.W., Jones, F.L., Powers, E.J., Kim, Y.C. and Khadra, L. 1982 Experiments on the role of amplitude and phase modulations during transition to turbulence. *J. Fluid Mech.* **123**, 1-20.

Patnaik, P.C., Sherman, F.S. and Corcos, G.M. 1976 A numerical simulation of Kelvin-Helmholtz waves of finite amplitude. *J. Fluid Mech.* **73**, 215-240.

Rajaee, M. and Karlsson, S.K.F. 1992 On the Fourier space decomposition of free shear flow measurements and mode degeneraring in the pairing process. *Phys. Fluids* **A 4**, 321-339.

Riley, J.J. and Metcalf, R.W. 1980 Direct numerical simulation of a perturbed mixing layer. *AIAA Paper* 80-0274.

Schwartz, Mischa 1990 Information transmission, modulation, and noise. 4th ed. New York: McGraw-Hill 264-279.

Shen, S.F. 1961 Some considerations on the laminar stability of time dependant basic flows. *Aerosp. Sci.* **28**, 397.

Teolis, A. 1997 Identification of Noisy FM signals using Non-Orthogonal Wavelet Transforms. *SPIE* **3078**, 592.

Yang, Z. and Karlsson, S.K.F. 1991 Evolution of coherent structures in a plane shear layer. *Phys. Fluids* **A 3**, 2207-2219.

Yuen, H.C., and Lake, B.H. 1975, Nonlinear deep water waves. theory and experiment. *Phys. Fluids* **18**, 956-960.

Vita

Craig Perry Lusk was born on November 1, 1973 in Salt Lake City, Utah. He is the fourth of four children in his family and the first in his family to receive a post-graduate degree. He graduated with honors from Radford High School in 1991. That same year he received his Eagle Scout Award. Craig received a National Merit Scholarship to attend Virginia Tech. He began his Bachelor's program in 1991. From May 1993 to May 1995, he served a mission for the Church of Jesus Christ of Latter-Day Saints in Washington State. There he learned Spanish and worked extensively with migrant workers. On December 21, 1996, Craig married Mary Kathleen Gilchrist. In 1997, Craig was accepted to a five year Bachelor's-Masters Program. On March 2, 1998, Craig and Mary were blessed with a healthy son, Kyle Ammon. In May 1998, Craig received his Bachelor's degree, Cum Laude, in Engineering Science and Mechanics with a minor in mathematics. In May 1999, Craig received his Masters degree in Engineering Mechanics.